

Light Management Strategies for Luminescent Solar Concentrators

A Thesis
SUBMITTED TO THE FACULTY OF
UNIVERSITY OF MINNESOTA
BY

Christian Pinnell

IN PARTIAL FULFILLMENT OF THE REQUIREMENTS
FOR THE DEGREE OF
MASTER OF SCIENCE

Dr. Vivian Ferry

September 2018

Acknowledgements

I would first like to thank my advisor Dr. Vivian Ferry. Her guidance and expertise in this field has been invaluable to my work. She has taught me how to ask the right questions throughout the research process, and to pursue the answers to those questions in rigorous detail. I would also like to thank Ryan Connell for teaching me about his work in LSCs and his aid in my simulations. His work and his knowledge in the field built a foundation from which I could pursue my own research. I would like to thank Dr. Mayank Puri for his aid in quantum dot synthesis. He has been always willing to help whenever I ask, and his instruction has aided me considerably in my experimental work. I would like to thank Dana Dement for her aid in ellipsometry measurements, and Samantha Hill for providing me with optical property data of her Si quantum dots. I'd also like to thank all of my other group members Matt Quan, Pavlos Pachidis, Ian Slauch, Bryan Cote, Chen Fan, and Sihoon Moon for their support throughout my research. Finally, I'd like to thank my committee members for agreeing to serve on my committee.

Dedication

To my Mom and Dad, who raised me to be the person I am today.

Abstract

This thesis explores three light management strategies for luminescent solar concentrators (LSCs). LSCs are concentrating photovoltaic systems in which luminophores are embedded within a polymer slab. Incident sunlight is absorbed by the luminophores, which then fluoresce. Fluorescent light is trapped within the polymer slab via total internal reflection and propagates to the edge of the slab where it is collected by solar cells. The first light management strategy uses wavelength-selective mirrors placed above the top surface of the concentrator to trap fluorescent light while transmitting sunlight in to be absorbed. Two mirrors are designed, and their performance is simulated when placed above a variety of LSCs. LSC parameters such as lateral size, quantum yield, and luminophore concentration were varied to study the effects of LSC design on top mirror design. The second strategy involves the use of multiple LSC layers for spectrum splitting. High energy light is absorbed by the top layer with minimal thermalization, while lower energy light is transmitted into the bottom layer, where it is absorbed. A multijunction LSC is modeled and its performance is simulated. Coupling effects between top and bottom layer performance are evaluated. Finally, the thin film architecture is considered, where a thin luminophore-quantum dot layer is deposited onto a glass substrate. A wave optics model is used to determine the effects of this architecture on luminophore emission and reabsorption. The performance of these LSCs are found to be superior to bulk polymer LSCs. Thin film LSCs are realized experimentally by synthesizing quantum dots and depositing a quantum dot-polymer layer onto a glass substrate. The optical properties of the quantum dots in solution and in the LSC are characterized and the light guiding properties of the thin film LSC are measured.

Table of Contents

List of Tables	v
List of Figures	vi
Chapter 1. Introduction	1
1.1 Motivation	1
1.2 Luminescent Solar Concentrators	2
1.3 Luminophores	4
1.4 Light Management Strategies for Luminescent Solar Concentrators	6
1.4.1 Wavelength-Selective Mirrors	6
1.4.2 Multijunction LSCs	7
1.4.3 Thin Film LSCs	10
1.5 Overview	12
Chapter 2. Wavelength-Selective Mirrors	13
2.1 Wavelength-Selective Mirror Design	13
2.2 Monte Carlo Algorithm	16
2.3 LSC Lateral Size	17
2.4 Luminophore Properties	21
Chapter 3. Multijunction Luminescent Solar Concentrators	25
3.1 Monte Carlo Algorithm Modifications	25
3.2 Light Absorption in Multijunction LSCs	27
3.2.1 First Pass through the Top LSC Layer	27
3.2.2 All Subsequent Passes Before the Mirror	30
3.2.3 First Set of Reflection Off Mirror	32
3.2.4 All Reflection Off Mirror	33
3.2.5 Total Absorption and Losses	36
3.2.6 Model Results and Monte Carlo Model Comparison	36
3.3 Multijunction LSC Simulations	37
3.3.1 Optical Density	37
3.3.2 Photoluminescent Coupling Effects	41
3.3.3 Ideal Top Mirrors	43
3.4 Multijunction LSC Performance	47
Chapter 4. Thin Film LSC Simulations	49
4.1 Ray and Wave Optics Model	49
4.2 Dipole Emission in a Homogeneous Medium and Dielectric Half Space	50
4.3 Dipole Emission in a Thin Film	54
4.3.1 Dipole Height and Orientation	54
4.3.2 Angular Distribution of Emission from a Dipole in a Thin Film	57
4.3.3 Reabsorption of Emission within a Thin Film	60
4.4 Thin Film Absorption, Reflection, and Transmission	62
4.5 Thin Film LSC Monte Carlo Simulations	65
Chapter 5. Thin Film LSC Experiments	70
5.1 CdSe/CdS Quantum Dot Synthesis	70
5.2 CdSe/CdS Quantum Dot Characterization	72
5.3 Thin Film Fabrication and Characterization	74
5.4 Effects of Thin Film Thickness on LSC Optical Properties	75
5.5 Light Guiding in Thin Film LSCs	78
Chapter 6. Conclusions and Future Work	80
6.1 Intermediate Reflectors for Multijunction LSCs	80
6.2 Thin Film LSCs	83
6.3 Conclusion	84
Bibliography	86

List of Tables

Table 3.1 Multijunction LSC Efficiencies.	48
---	----

List of Figures

Figure 1.1 LSC Diagram.....	2
Figure 1.2 LSC Loss Mechanisms.....	3
Figure 1.3 CdSe/CdS and Si Absorption and Emission Spectra.....	4
Figure 1.4 Wavelength-Selective Mirror Reflection Spectrum.....	7
Figure 1.5 Multijunction Benefits.....	8
Figure 1.6 Multijunction LSC Diagram.....	9
Figure 1.7 Solar Spectrum with Absorption Bands.....	10
Figure 1.8 Thin Film Benefits.....	11
Figure 2.1 Aperiodic Mirror Reflection Spectra.....	15
Figure 2.2 Monte Carlo Algorithm.....	16
Figure 2.3 Concentration Factor.....	18
Figure 2.4 Optical Efficiency at Varying Lateral Sizes.....	20
Figure 2.5 Absorption with Varying Luminophores.....	22
Figure 2.6 Optical Efficiency at Varying Optical Densities.....	23
Figure 2.7 Concentration Factor at Varying Quantum Yield.....	24
Figure 3.1 Multijunction LSC System.....	26
Figure 3.2 Analytical Model for Absorption—Top.....	28
Figure 3.3 Analytical Model for Absorption—Middle.....	31
Figure 3.4 Analytical Model for Absorption—Bottom.....	32
Figure 3.5 Monte Carlo and Analytical Model Absorption.....	36
Figure 3.6 Multijunction LSC Performance with Optical Density.....	38
Figure 3.7 Bottom Layer Performance with Optical Density.....	39
Figure 3.8 Multijunction LSC Edge Collection.....	41
Figure 3.9 Photoluminescent Coupling.....	42
Figure 3.10 Idealized Top Mirrors.....	44
Figure 3.11 Multijunction LSC Performance with Idealized Top Mirrors.....	45
Figure 4.1. Angular Distribution of Emission in a Homogeneous Medium.....	52
Figure 4.2. Angular Distribution of Emission Near a Half-Space.....	54
Figure 4.3 Emission for Varying Dipole Orientations.....	55
Figure 4.4 Angular Distribution of Emission for Varying Heights.....	56
Figure 4.5 Angular Distribution of Emission in a Thin Film.....	58
Figure 4.6 Angular Distribution of Emission at Varying Thin Film Thicknesses.....	59
Figure 4.7 Thin Film Reabsorption.....	61
Figure 4.8 Analytical Model for Thin Film Absorption, Reflection, Transmission.....	62
Figure 4.9 Thin Film LSC Collection Mechanisms.....	66
Figure 4.10 Thin Film and Bulk Polymer LSC Performance.....	67
Figure 4.11 Thin Film and Bulk Polymer Escape Cone and Reabsorption Losses.....	68
Figure 5.1 CdSe Quantum Dot Absorption.....	71
Figure 5.2 CdSe/CdS Quantum Dots TEM Images.....	72
Figure 5.3 CdSe/CdS Solution State Absorption and Emission Spectra.....	73
Figure 5.4 CdSe/CdS Solid State Emission Spectrum.....	74
Figure 5.5 Thin Film LSC Extinction Spectrum.....	75
Figure 5.6 Thin Film LSC Refractive Index.....	76
Figure 5.7 Angle-Resolved Reflection.....	77
Figure 5.8 Attenuation Measurements.....	79
Figure 6.1 Wavelength-Selective Intermediate Reflectors for Multijunction LSCs.....	81
Figure 6.2 Metasurface Intermediate Reflectors for Multijunction LSCs.....	83

Chapter 1. Introduction

1.1 Motivation

The development of photovoltaics for solar energy harvesting continues to be a critical field of research. In 2017, 65 billion kilowatt hours of solar energy was generated [1], and solar energy generation is projected to rise to 400 billion kilowatt hours by 2040 [2]. Photovoltaic efficiency improvements can be achieved while maintaining low costs through the concentration of light onto photovoltaics, as solar cells operate at higher efficiencies under concentrated illumination [3]–[6]. Concentrating systems for photovoltaics have been an active area of research over the past several decades [7]–[12]. These systems concentrate sunlight onto small, high efficiency solar cells, reducing the usage of expensive solar cell materials while increasing the efficiency of the solar cells by increasing their short circuit currents.

Parabolic dish concentrators are the most commonly used class of concentrator for photovoltaics [13]–[15]. These concentrators exhibit good performance for direct sunlight, but they are unable to effectively collect diffuse light [5], [7], [8], [14]. As diffuse light constitutes 10–20% of all solar radiation on clear days, and up to 100% on cloudy days [16], this significantly reduces the overall performance of these systems. Consequently, parabolic dish concentrators require expensive, bulky solar tracking systems [6]–[8], [14]. In contrast, luminescent solar concentrators (LSCs) effectively concentrate both direct and diffuse sunlight [15], [17], [18]. LSCs also concentrate light spectrally, focusing broadband sunlight to a narrow range of wavelengths. This allows concentrated light to be matched to the peak external quantum efficiency of the solar cell. LSCs can be easily integrated into

building architectures and can provide heat management benefits, making them attractive options for concentrating photovoltaics.

1.2 Luminescent Solar Concentrators

Luminescent solar concentrators consist of a slab of optically transparent material, typically a polymer, embedded with luminescent materials, known as luminophores, with solar cells fastened to the edges of the slab. Figure 1.1 shows a diagram of an LSC. Luminophores in the slab absorb incident sunlight and subsequently emit light which is then guided via total internal reflection to the edges, where it is collected by the solar cells. Since the LSC is thin relative to its lateral dimensions, this device acts as a solar concentrator.

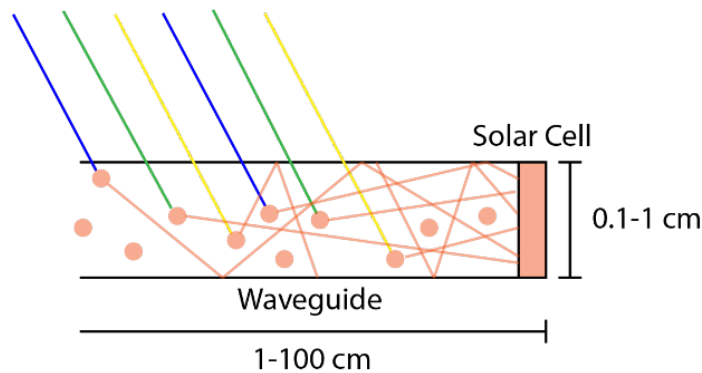


Figure 1.1 Sunlight incident upon the LSC is absorbed by the luminophores. Fluorescent light is emitted by the luminophores and trapped via total internal reflection. Trapped light is guided to the edge of the device, where it is collected by edge-mounted solar cells.

Numerous loss mechanisms exist in LSCs which reduce the collection of light by solar cells. Much of the research in LSCs aims to minimize these losses, thereby increasing LSC efficiency. Figure 1.2 summarizes common loss mechanisms considered here. When

light is absorbed by luminophores, not all the light will be converted to emitted photons, as luminophore quantum yield is less than 100%. Some of the light will be lost to non-radiative recombination. These losses are called absorption losses. Light that is emitted can be reabsorbed by other luminophores if there is overlap between luminophore absorption and emission bands. Light that is emitted, reabsorbed, and lost to non-radiative recombination constitute reabsorption losses. A third type of losses are escape cone losses, which occur when light is emitted into the escape cone rather than a total internal reflection mode. For an isotropically-emitting luminophore in a layer with refractive index 1.49, 74% of emitted light is trapped [19]. This means 26% is emitted into the escape cone. The fraction of light emitted into the escape cone, P , for a concentrator with refractive index n is given in Equation 1.1 [20]. The last two loss mechanisms deal with light which is not absorbed at all. Light may be reflected off the top surface of the concentrator, called reflection losses, or pass through without being absorbed, called unabsorbed losses.

$$P = 1 - \sqrt{1 - 1/n^2} \quad (1.1)$$

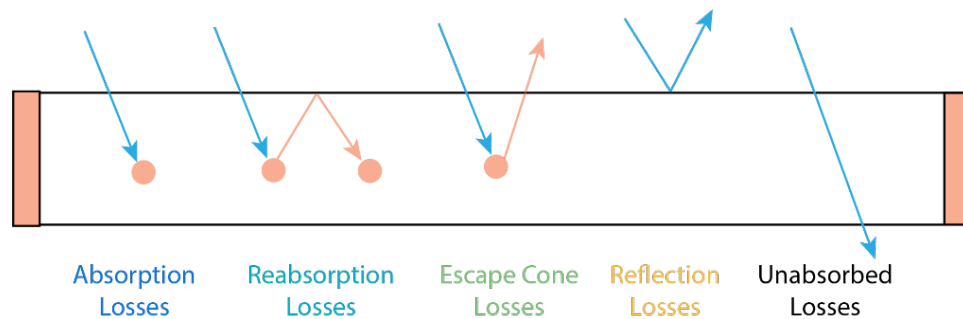


Figure 1.2 The common loss mechanisms in an LSC are given. Light can be absorbed or reabsorbed and lost to non-radiative recombination. Light can be emitted into the escape cone, where it is not trapped via total internal reflection. Light can also remain unabsorbed, either passing through the concentrator without being absorbed or getting reflected off the top surface of the concentrator.

1.3 Luminophores

Luminophores are a central component of the LSC, as the choice of luminophore can impact device performance significantly. Luminophores should be able to absorb high energy sunlight while efficiently emitting light. They should have little spectral overlap, where the emission spectrum is significantly red-shifted with respect to the absorption spectrum to minimize reabsorption. Additionally, the luminophores should be photostable, inexpensive, and non-toxic. The most common classes of luminophores used in LSCs are fluorescent dyes [4], [10], [11], [18], [21]–[23] and quantum dots [4], [10], [11], [17], [24].

CdSe/CdS core-shell quantum dots and Si quantum dots are chosen for this work. CdSe/CdS quantum dots are attractive luminophores for LSC applications due to their high quantum yield, small spectral overlap, narrow emission spectrum, and photostability. Meanwhile, Si quantum dots possess a very little spectral overlap due to their indirect

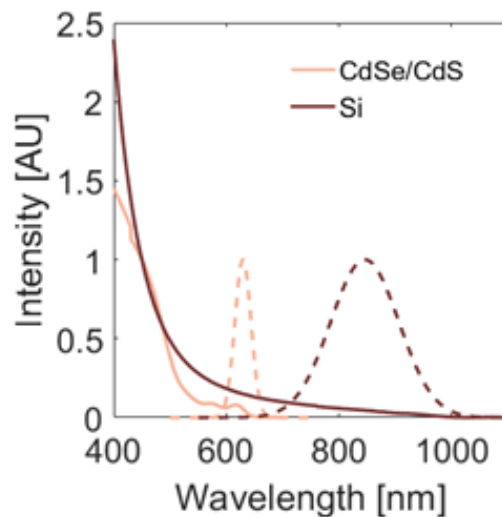


Figure 1.3 Absorption (solid) and emission (dotted) spectra are shown. CdSe/CdS quantum dots (pink) possess a narrow emission spectrum. Si quantum dots (maroon) have little overlap between their absorption and emission spectra. The Si absorption and emission spectra are courtesy of Samantha Hill.

bandgap and are made from inexpensive, nontoxic, and earth-abundant materials. The absorption and emission spectra for CdSe/CdS and Si quantum dots are shown in Figure 1.3. The optical properties of Si quantum dots are courtesy of Samantha Hill.

In this work, both single layer and multijunction LSCs are examined. Multijunction LSCs, discussed in Section 1.4.2, feature multiple absorbing layers which are stacked to form a multijunction architecture. Different luminophores are placed in each layer to achieve spectrum splitting, where high energy light is absorbed by the top layer and lower energy light is absorbed by the lower level. Multijunction LSCs in the current work use CdSe/CdS quantum dots in the top layer and Si quantum dots in the bottom layer. A detailed balance shows the ideal bandgaps for the top and bottom junctions of a two-junction solar cell are 1.9 and 1.0 eV, respectively [25]. As an analogous system, luminophores in a two-junction LSC should have the same bandgaps. The CdSe/CdS quantum dots used here have a bandgap of 2.1, making them a good candidate for the top layer.

Although the Si quantum dots used in the preliminary work have a band gap greater than 1.0 eV, Si quantum dots have been made with bandgaps between 1.0–1.2 eV [26]–[28], and other candidate small band gap luminophores come with significant drawbacks. Near-infrared emitting fluorescent dyes suffer from prohibitively low quantum yields [29], [30]. Small band gap quantum dots such as PbS and PbSe are toxic, have low Stokes shifts and show photobleaching [31]–[33]. Adding a PbS shell to PbSe cores increases photostability but decreases quantum yield and Stokes shift [34]–[36]. CuInSe/ZnS

core/shell quantum dots have moderate quantum yield but low Stokes shift and blue-shifted emission relative to Si quantum dots [29], [37].

1.4 Light Management Strategies for Luminescent Solar Concentrators

The loss mechanisms discussed in Section 1.2 contribute to significant losses in LSC efficiency. These efficiency losses can be mitigated by improvements in luminophore optical properties, for instance by increasing quantum yield or decreasing spectral overlap, or by the implementation of light management strategies which manipulate the light-matter interactions within the LSC. Multiple light management strategies for LSCs are examined in this work, including the use of wavelength-selective mirrors, multijunction architectures, and the use of thin film architectures to control the angle of light emission. Each of these areas is briefly introduced below and discussed in more detail in later chapters.

1.4.1 Wavelength-Selective Mirrors

Escape cone losses present a major loss mechanism in LSCs. Literature shows decreases in these losses upon the addition of wavelength-selective mirrors above the top surface of the LSC [10], [11], [15], [17]–[19], [21], [38], [39]. These mirrors selectively transmit high energy photons which are readily absorbed by the LSC while reflecting low energy photons emitted by the luminophore. Utilizing these mirrors, the concentrator can maintain high light absorption and dramatically increase the trapping of emitted light. Simulations have shown a 50% increase in LSC output for an ideal wavelength-selective mirror, and 20% increases have been realized experimentally [10]. Theoretical work by Rau et al. has shown that a wavelength-selective mirror is required for LSCs to reach their potential [38]. Experimentally, these mirrors are often made from 1D photonic crystals

(PCs), such as Bragg stacks [40] and Rugate filters [19], [41]–[43], or 3D PCs in opal or inverted opal geometries [19], [40], [44]–[49].

An aperiodic reflector is used in the present work as a top mirror to reduce escape cone losses in an LSC. These mirrors are similar to Bragg stacks, which feature repeating layers of high and low index of refraction dielectric layers. However, while Bragg stacks have periodic layer thicknesses, the thickness of each layer in an aperiodic filter is tuned to reduce reflection outside of the desired wavelength range. Figure 1.4 shows the reflection spectrum of an aperiodic top mirror overlaid with the absorption and emission spectrum of CdSe/CdS quantum dots.

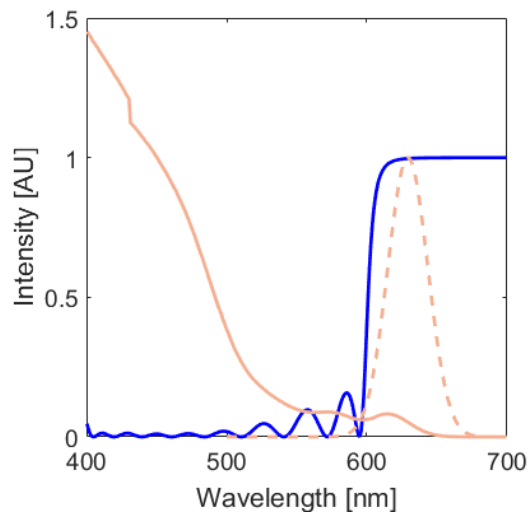


Figure 1.4 The reflection spectrum of an aperiodic wavelength-selective mirror (blue) is overlaid against the absorption (pink, solid) and emission (pink, dotted) spectra of CdSe/CdS quantum dots. High energy light is transmitted through the mirror to be absorbed, while lower energy emitted light is reflection and trapped.

1.4.2 Multijunction LSCs

Thermalization due to the absorption of light with energy above the band gap leads to major energy losses in photovoltaics and LSCs alike. When photons with energy higher

than the bandgap are absorbed, excited electrons create phonons as they relax to the band edge. These phonons dissipate as heat, which provides unwanted heating of the system and reduces efficiency [50], [51]. For an ideal solar cell with a band gap of 1.0 eV, 37% of incident solar energy is lost to these thermalization losses. Semiconductor materials with larger band gaps can be chosen to reduce thermalization, but these materials limit the spectral range of light available for absorption since light with energy lower than the band gap is readily not absorbed.

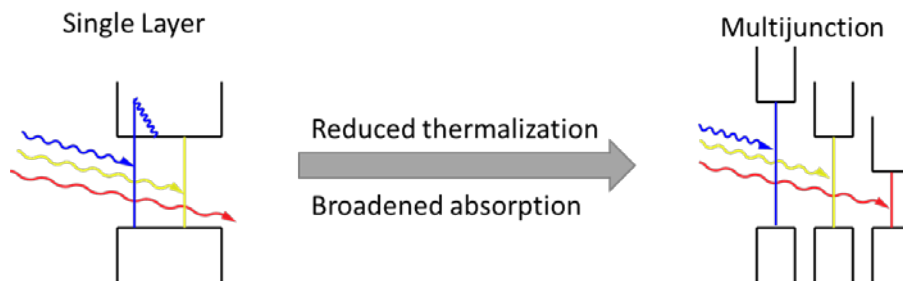


Figure 1.5 Multijunction LSCs reduce thermalization and broaden absorption by stacking LSC layers with different luminophores in order of band gap. Luminophores with larger band gaps are placed at the top of the stack to absorb high energy light with minimal thermalization. Lower band gap materials absorb lower energy light transmitted by the upper layers.

Multijunction geometries minimize thermalization while maintaining a wide spectral absorption range. In multijunction photovoltaics, solar cells with increasing band gaps are stacked, with the smallest band gap on the bottom [52]. The first junction absorbs high energy light with minimal thermalization, while lower energy light is absorbed by successive junctions, maintaining the wide spectral absorption range of the bottom solar cell. The addition of a 1.9 eV junction to an ideal 1.0 eV solar cell decreases thermalization losses by over 40% while continuing to absorb light with energy greater than 1.0 eV.

Multijunction solar cells have reached efficiencies of 46.0%, the most efficient solar cell to date [53], [54].

Multijunction LSC architectures, shown in Figure 1.6, can be used similarly to decrease thermalization and widen the spectral absorbance range [55], [56]. In these systems two or more absorbing layers with different luminophores are stacked. Separate solar cells are attached to the edges of each layer, allowing the peak external quantum efficiency of the solar cell to be matched to the emission spectrum of each luminophore.

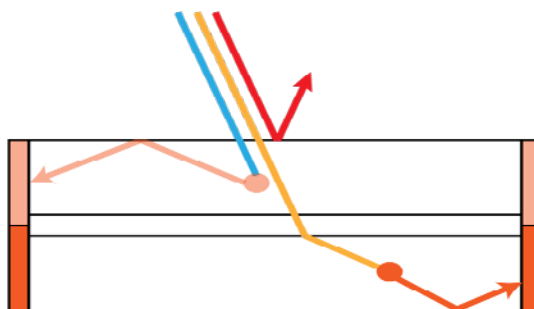


Figure 1.6 Different solar cells are attached to the top (pink) and bottom (orange) layers of the multijunction LSC. Mirrors can be placed at the front and back of the multijunction LSC to trap emitted light. Intermediate reflecting layers can be added for light manipulation, such as high angle diffraction to increase path length and therefore, absorbance.

Multijunction LSCs in the current work use CdSe/CdS quantum dots in the top layer and Si quantum dots in the bottom layer. Absorption in the CdSe/CdS top layer should be small at wavelengths longer than 600 nm to minimize overlap between the absorption and emission spectra of the CdSe/CdS quantum dots. Since absorption is approximately constant between 525 nm and 600 nm, this means the top layer should be designed to absorb light effectively at wavelengths shorter than 525 nm, which constitutes 22.4% of incident solar energy. Similarly, Si layer absorption should be small at wavelengths longer

than 700 nm, making 525–700 nm the desired range for bottom layer absorption. This wavelength range contains 25.1% of incident solar energy, as shown in Figure 1.7.

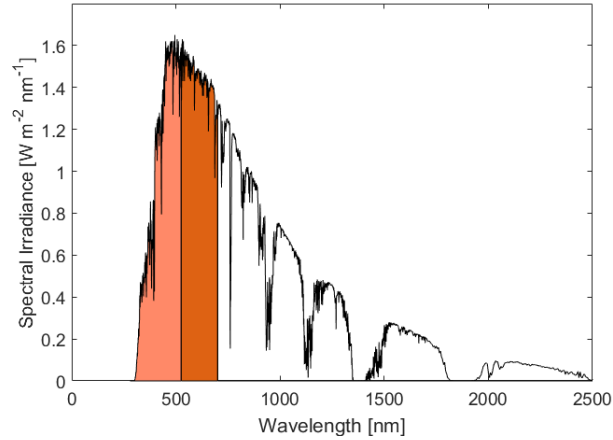


Figure 1.7 The AM1.5 Global solar spectrum is shown. 22.4% of incident solar energy is available to the CdSe/CdS layer (shaded in pink). 25.1% of incident solar energy is available to the Si layer (shaded in orange).

1.4.3 Thin Film LSCs

LSCs typically consist of luminophores embedded in polymer slab. However, luminophores can also be embedded into a thin polymer film deposited onto a glass substrate. The thin film architecture offers several benefits for LSC performance over polymer slab LSCs. In bulk polymer concentrators, emitted light is trapped within the absorbing layer and can be readily reabsorbed by other luminophores or scattered by the polymer matrix or luminophore aggregates. Thin film concentrators reduce reabsorption by confining absorption to a thin polymer layer while trapped light propagates primarily through a non-absorbing glass substrate with little scattering [57].

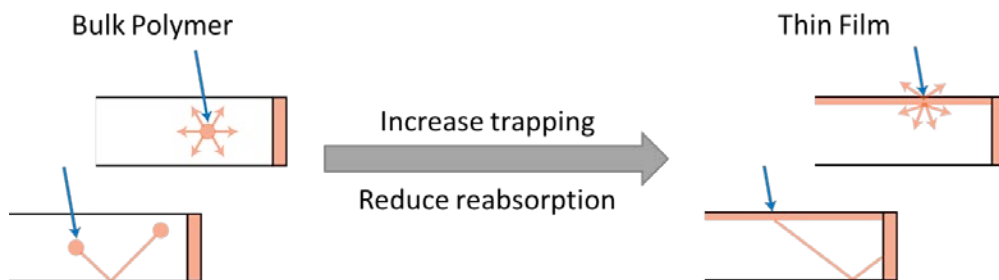


Figure 1.8 Thin film LSCs reduce escape cone losses by preferentially emitting light into total internal reflection modes. Reabsorption losses are reduced by confining the absorbing layer to a thin quantum-dot polymer film, allowing trapped light to propagate primarily through a non-absorbing glass substrate.

In addition to light guiding benefits, the thin film architecture reduces escape cone losses by altering luminophore emission. Light emission from luminophores in a homogeneous medium is isotropic, with each angle receiving equal emission intensity. Luminophores in an inhomogeneous medium, however, emit light anisotropically [58]–[62]. Thin film LSCs have film thicknesses similar to the wavelength of emitted light, meaning luminophores in the polymer film are in an inhomogeneous medium. Dipoles in a thin film are known to emit light preferentially into the higher refractive index surroundings at steep angles [58], [59]. In a thin film LSC, light emitted from the thin film is emitted preferentially into the glass substrate at steep angles and is trapped in the substrate via total internal reflection, allowing it to propagate to the edge of the concentrator. In this work, CdSe/CdS quantum dots are embedded into poly(cyclohexylethylene) (PCHE). PCHE is chosen as it is an optically clear polymer with minimal scattering, and it is soluble in the nonpolar solvents used to synthesize the quantum dots. Thin film LSCs are created by placing a quantum dot-polymer thin film onto a glass substrate.

1.5 Overview

Three light management strategies for LSCs are designed and evaluated in this thesis. Monte Carlo ray-tracing simulations are used to study the effects of these strategies on concentrator performance. Chapter 2 focuses on the use of wavelength-selective top mirrors to increase light trapping in LSCs. Various LSCs with top mirrors are modeled and compared to determine how concentrator design influences the design of these mirrors. Chapter 3 discusses the use of a multijunction architecture to increase light absorption and decrease thermalization. Two-layer LSCs are modeled using CdSe/CdS and Si quantum dots as luminophores. The interdependence of layer performance is examined using a modified ray-tracing algorithm and the design of wavelength-selective mirrors for a multijunction system is briefly discussed. In Chapter 4, the thin film LSC architecture is explored using simulations. FDTD calculations are used to study the emissive properties of quantum dots in a thin film. A ray-tracing model is then used to compare thin film and bulk polymer LSC performance. Chapter 5 focuses on experimental work with thin film LSCs. CdSe/CdS quantum dots are synthesized using a colloidal synthesis. Thin film LSCs are fabricated by spin coating a quantum dot-polymer layer onto a glass substrate. The optical properties of the thin films are characterized and attenuation experiments are performed to study the light guiding properties of the LSCs. Finally, conclusions from this thesis and suggestions for future work on multijunction and thin film LSCs are presented in Chapter 6.

Chapter 2. Wavelength-Selective Mirrors

Wavelength-selective mirrors which transmit light across the absorption band of the luminophore while reflecting light across the emission band of the luminophore are crucial to the reduction of escape cone losses in LSCs. The addition of such a mirror above the top surface of an LSC is required to achieve maximum efficiency [38]. The design of these mirrors, however, is difficult as overlap between the absorption and emission spectra of the luminophore creates a tradeoff between the transmission of sunlight into the concentrator and the trapping of luminescent light within the concentrator [63]. Mirror design is further complicated as the one-dimensional mirrors often used for this purpose have reflectivity bands which blue-shift as angle of incidence shifts away from normal incidence. In this section, the tradeoff between sunlight transmission and trapping of luminescent light in wavelength-selective mirrors is explored for various LSCs, and we show how LSC lateral size, luminophore, luminophore concentration, and quantum yield influence the design of these wavelength-selective mirrors.

2.1 Wavelength-Selective Mirror Design

A series of one-dimensional, aperiodic mirrors are designed to reduce escape cone losses in an LSC. These mirrors feature alternating dielectric layers of refractive index 1.45 and 2.53. An aperiodic stack is chosen to reduce reflection outside of the desired reflection band, which is prominent in periodic stacks. The thicknesses of each layer in the stack is varied to tune the location of the mirror's reflection band. An optimization method using the refractive index of each layer, the absorption and emission spectra of the luminophore, and initial guesses for layer thickness is used to determine the thickness of each layer.

Layer thickness in a periodic 1D Bragg stack, the peak wavelength of the emission spectrum divided by four times the refractive index of the layer, are used as initial guesses for layer thickness. A figure of merit is used to optimize mirror design. This figure of merit takes into consideration overlap between the reflection band and the absorption band, and overlap between the reflection band and the emission band.

$$FOM = \left(\frac{1}{A}\right)^{W_a} \left(\frac{1}{E}\right)^{W_e} \quad (2.1)$$

where A and E are parameters representing reflection across the absorption and emission bands, respectively, and W_a and W_e are weighting factors for the absorption and emission terms.

The absorption parameter is calculated by integrating the product of top mirror transmission at normal incidence and the absorption band of the luminophore over the absorption band, weighting by the solar spectrum.

$$A = \frac{\int_{\lambda_{A,min}}^{\lambda_{A,max}} (1 - R_{TopMirror}(\theta=0, \lambda)) \alpha(\lambda) P_{ss}(\lambda) d\lambda}{\int_{\lambda_{A,min}}^{\lambda_{A,max}} \alpha(\lambda) P_{ss}(\lambda) d\lambda} \quad (2.2)$$

The emission parameter is calculated by integrating the product of top mirror reflection and the emission band of the luminophore over the emission band and emitted angles.

$$A = \frac{\int_{\lambda_{A,min}}^{\lambda_{A,max}} \int_0^{\frac{\pi}{2}} R_{TopMirror}(\theta, \lambda) PL(\lambda) \sin(\theta) d\theta d\lambda}{\int_{\lambda_{A,min}}^{\lambda_{A,max}} \int_0^{\frac{\pi}{2}} PL(\lambda) \sin(\theta) d\theta d\lambda} \quad (2.3)$$

By varying the absorption and emission weighting factors, mirrors are designed with different reflection bands, as shown in Figure 2.1. In this figure, the reflection band

at normal incidence of several mirrors is overlaid against the absorption and emission spectra of CdSe/CdS quantum dots with a seven monolayer CdS shell.

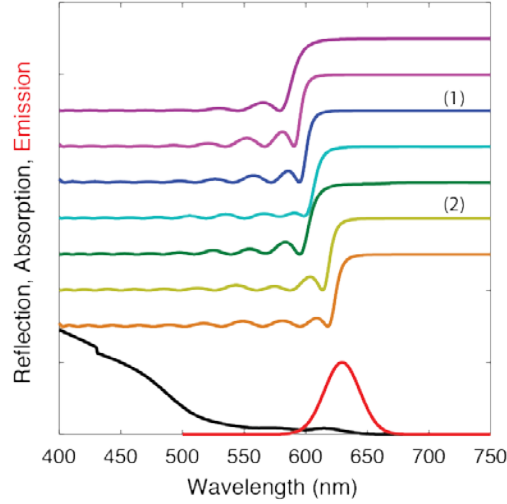


Figure 2.1 Reflection bands for different mirrors at normal incidence are given. Overlaid is the absorption (black) and emission (red) spectra of a CdSe/CdS quantum dots with a seven monolayer shell. The mirror labeled (1) is referred to as the emission weighted mirror. The mirror labeled (2) is referred to as the absorption weighted mirror.

Of the mirrors shown in Figure 2.1, two are selected for further study. The mirror labeled (1) in Figure 2.1 is chosen to represent emission weighted mirrors designed to preferentially trap emitted light, while the mirror labeled (2) in Figure 2.1 is chosen to represent absorption weighted mirrors designed to preferentially transmit light across the absorption band. These particular mirrors are chosen as they exhibit local maxima in LSC performance for concentrators with lateral dimensions 1 m x 1 m, quantum yield 0.9, and optical density 0.5 at 450 nm.

2.2 Monte Carlo Algorithm

A ray-tracing Monte Carlo model is used to simulate LSC performance. Monte Carlo simulations have been used extensively in LSC studies to examine a variety of luminophores and LSC designs [37], [64]–[66]. This ray-tracing model uses angle- and wavelength-dependent reflectivity of the aperiodic mirrors, reflective and scattering properties of the back mirror, LSC geometry, and optical properties of the luminophore and polymer to predict the interaction of light with the concentrator system.

In present studies, photons of a specified wavelength range are injected above the top face of the LSC and tracked. The simulations are discretized in time, where for each time step the photon moves a distance equal to the product of the speed of light and the time step. As photons propagate through the system, they may reach an interface between materials, where they could be reflected or refracted. Fresnel equations are used to determine the probability of reflection and Snell's Law is used to determine the direction of refracted light [67]. Photons within the concentrator may be absorbed, where the

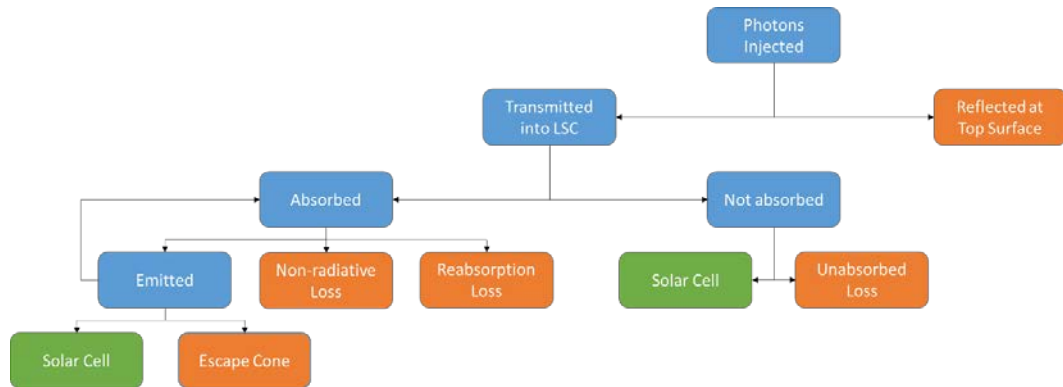


Figure 2.2 A flow chart of the Monte Carlo algorithm used in ray-tracing simulations is given. Blue marks non-collection events. Loss mechanisms are shown in orange, while light collected by edge-mounted solar cells are marked in green.

probability of absorption is calculated from experimental absorption data for the luminophore and using Beer's Law [68]. Upon absorption, a photon may be emitted at a random angle and a new wavelength determined by the emission spectrum, or lost to absorption or reabsorption losses due to non-unity quantum yield. The simulation continues to run until all photons have reached a collection mechanism.

A flow chart of the Monte Carlo algorithm is given in Figure 2.2. Photons which reach the edge of the concentrator are collected by the solar cell, shown in green, while other photons are collected by loss mechanisms, shown in orange. Lost photons include photons reflected off the top surface of the concentrator or top mirror, lost to non-radiative recombination upon the first absorption event (non-radiative losses) or subsequent absorption events (reabsorption losses), emitted into the escape cone, or pass through the concentration unabsorbed. The number of photons collected by each collection mechanism is tracked to determine LSC performance.

2.3 LSC Lateral Size

Wavelength-selective mirrors are critical for the reduction of escape cone losses in LSCs. Aperiodic mirrors contain a reflection band across a desired spectral range with little reflection outside of this range, making it possible to effectively reflect light across the emission band of an LSC while transmitting light across its absorption band. Overlap between the absorption and emission bands presents a tradeoff in mirror design between transmitting and trapping light. While it is important to study this tradeoff for small, lab scale concentrators, it is also important to study how it changes with scaling to large concentrator sizes. As LSC lateral size is scaled, photons must travel longer average

distances to reach the edge of the device, changing the trapping and guiding properties of the concentrator. This inevitably alters mirror design. Monte Carlo simulations are used here to explore the effects of LSC lateral size on LSC performance and aperiodic mirror design.

Three concentrator systems are chosen with different top mirrors. Each system contains CdSe/CdS quantum dot luminophores with a quantum yield of one and a diffuse back mirror which reflects light at all angles with equal intensity. The first system contains no top mirror, referred to as the standard LSC, while the second and third systems contain periodic and aperiodic top mirrors, respectively. The concentration factor of each system as LSC lateral size is scaled from 10^{-2} m to 10^2 m is shown in Figure 2.3. Concentration factor is a measure of the ability of an LSC to concentrate light, defined as the product of optical efficiency and geometric gain factor [69].

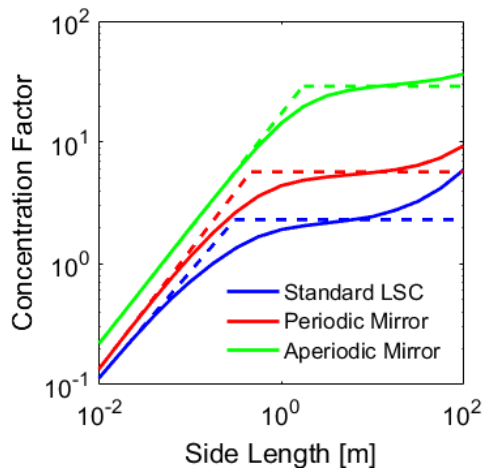


Figure 2.3 Concentration factor is plotted against side length for three LSC systems. The standard LSC (green) has no top mirror, while the second (red) and third (blue) LSCs have periodic and aperiodic top mirrors, respectively. Each LSC has a diffuse back mirror. Dotted lines mark the linear regime at short side lengths, and the horizontal regime at large side lengths.

As concentrator side length is varied, two regimes are observed, marked by sloped and horizontal lines in Figure 2.3. At small side lengths, concentration factor rises linearly with lateral size as geometric gain factor increases with little change in optical efficiency. For moderate side lengths, increases in geometric gain factor balance out with decreases in optical efficiency to form a constant concentration factor regime. Photons traveling farther average distances to reach the edge are more susceptible to reabsorption and hence reabsorption losses. Increasing concentration factor at large side lengths is observed due to a saturation of reabsorption losses as some emitted light is outside the absorption band of the luminophores. This behavior at large side lengths may not be a realistic prediction because the model does not account for light scattering by the polymer matrix, which may become significant for very large LSCs.

The lateral size at which the linear and horizontal concentration factor regimes meet is referred to as the saturation length of the concentrator [65]. A large saturation length indicates the effective trapping and guiding of light in the LSC, as long side lengths are required to observe significant escape cone and reabsorption losses. Upon the addition of a periodic reflector the saturation length of the LSC increases from 0.309 m to 0.463 m. While a moderate increase in saturation length was observed for a periodic reflector, imperfect reflection within the desired reflection band and undesired reflection outside of it limit the effectiveness of the mirror. A much larger improvement, to 1.855 m, is seen for an aperiodic reflector due to its optimized reflection spectrum, maintaining high absorption and decreasing escape cone losses.

The impact of lateral size on aperiodic mirror design is determined by comparing concentrators with the absorption weighted and emission weighted mirrors, as discussed in Section 2.1, added above the top surface. Figure 2.4 shows the optical efficiency of concentrators with each mirror (a). Mirror design shifts from absorption weighted mirrors for small concentrators to emission weighted mirrors at larger sizes, with a crossover point at 0.1 m. Absorption efficiency is independent of lateral size, as light absorption is determined by thickness of the concentrator, not its lateral size. Trapping efficiency, on the other hand, is dependent on LSC lateral size. In small concentrators, light emitted into a total internal reflection mode has a small average distance required to reach the edge, meaning photons can be collected with little interaction with the mirror. Therefore, escape cone losses are small for concentrators with either absorption or emission weighted mirrors. This is evident in Figure 2.4(b), which shows that trapping efficiency is near unity for both mirrors at small sizes. Consequently, as both mirrors efficiently trap light in the LSC, allowing as much light into the concentrator as possible results in the largest optical

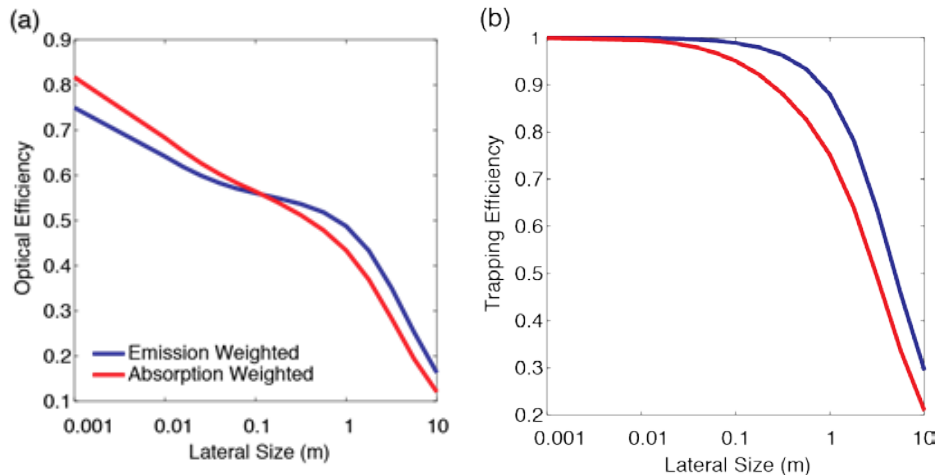


Figure 2.4 The optical efficiency of LSCs with an emission (blue) or absorption (red) weighted mirror is given in (a). (b) The trapping efficiency of LSCs with each mirror is shown.

efficiency. Since the absorption weighted mirror is designed to preferentially allow light in, larger optical efficiencies for this reflector is observed.

At large lateral sizes photons experience more interactions with the mirrors, as they must travel longer average distances to reach the edge. This is evidenced by the sharp drop in trapping efficiency at larger sizes for both mirrors (Figure 2.4(b)). As a result, mirrors that most effectively trap light are able to guide the most light to the edge. The emission weighted mirror is designed to do just this, so it is preferred to the absorption weighted reflector for large lateral sizes.

2.4 Luminophore Properties

In addition to LSC lateral size, the choice of luminophore, concentration of luminophore within the concentrator, and quantum yield of the luminophore have implications for the design of wavelength-selective top mirrors and are studied.

All luminophores have distinct absorption and emission spectra, making mirror design dependent on the choice luminophore. Three Cd-based quantum dots are used here to determine the impact absorption and emission spectra overlap. CdSe core particles are shelled with zero, three, or seven monolayers of CdS. As shell thickness increases, excitonic features near the edge of the absorption band are suppressed, reducing overlap. Mirrors are designed for LSCs with these luminophores, each with quantum yield 0.9, optical density 1 at 450 nm, and a lateral size of 1 m x 1 m.

For luminophores with significant overlap, transmitting light into the concentrator is more important than trapping emitted light. Figure 2.5 shows the absorption within the concentrator for each system. Mirrors for concentrators with CdSe and CdSe/3ML CdS

quantum dots preferentially transmit light, leading to high absorption and low trapping. Emitted photons in these systems are more likely to be reabsorbed and therefore less likely to interact with the mirror, decreasing the importance of trapping. Meanwhile, mirrors designed for concentrators with luminophores having little overlap show preferential trapping, with lower absorption and higher reflection, as emitted photons are very likely to interact with the mirror.

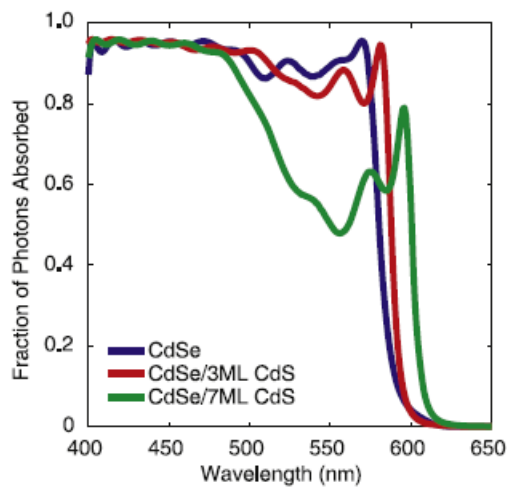


Figure 2.5 The fraction of incident light absorbed at each wavelength is shown for LSCs with CdSe/CdS quantum dots with zero (blue), three (red), and seven (green) monolayers of CdS.

The concentration of luminophores in a concentrator directly correlates to absorption of light by the concentrator, and reabsorption losses within the concentrator. Concentrators with optical densities between 0.1 and 2.0 at 450 nm, a quantum yield of 0.9 and a lateral size of 1 m x 1 m were simulated. As optical density is increased, a rise and eventual fall in optical efficiency is observed for concentrator with either mirrors, shown in Figure 2.6. At low concentrations, the increase in absorption associated with an increase in optical density outweighs the effects of reabsorption. However, as absorption saturates

at high concentrations, reabsorption losses continue to rise, leading to decreasing optical efficiency.

The emission weighted mirror outperforms the absorption weighted mirror at low concentrations. The performance of the absorption weighted mirror overtakes that of the emission weighted mirror at an optical density around 1.4. As with large spectral overlap, for concentrators with high luminophore concentrations, emitted light is likely to be reabsorbed and therefore less likely to interact with the mirror, leading to an emphasis on transmission over trapping.

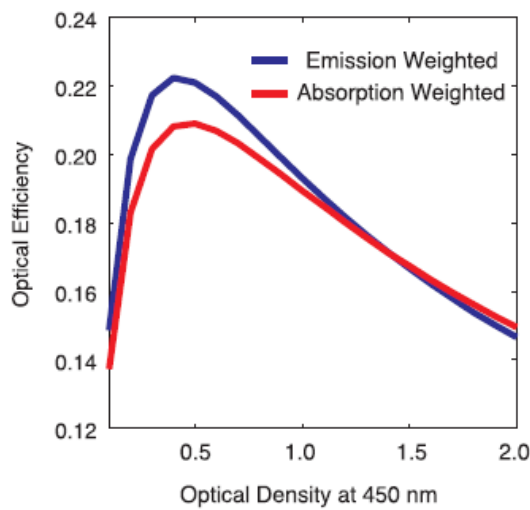


Figure 2.6 The optical efficiency for concentrators with emission (blue) and absorption (red) weighted mirrors is compared with varying optical density at 450 nm.

Lastly, luminophore quantum yield is varied for concentrators without a top mirror and with either the absorption or emission weighted top mirrors. Both mirrors are seen to give a boost in performance over the concentrator without a mirror, shown in Figure 2.7. Although the absorption and trapping efficiency is different for each mirror, the

performance of the mirrors is similar for quantum yields under 85%. Only at high quantum yields does the emission weighted mirror become preferred due to the high number of interactions a photon has with the mirror as reabsorption losses approach zero (unity quantum yield).

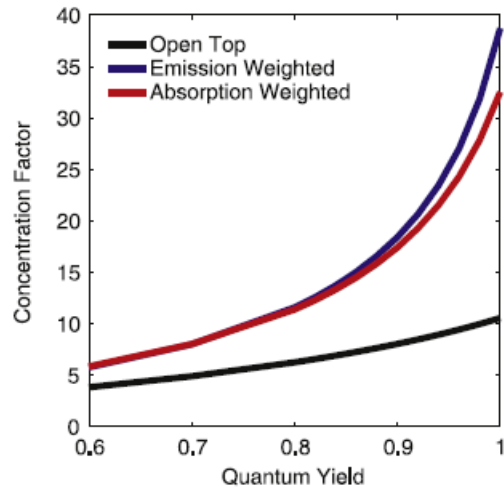


Figure 2.7 Concentration factor is given as a function of luminophore quantum yield. LSCs with no top mirror (black), an emission weighted mirror (blue), and an absorption weighted mirror (red) are compared.

Chapter 3. Multijunction Luminescent Solar Concentrators

LSCs suffer from thermalization losses when photons with energy higher than the band gap of the luminophore are absorbed. The resulting exciton quickly relaxes to the band edge, releasing a fraction of its energy as phonons which dissipate as heat. This loss in energy can be mitigated through the use of higher band gap luminophores. However, these luminophores suffer from lower absorption as no photons with energy lower than the band gap can be absorbed. Stacking LSC layers with different band gap luminophores allows for the reduction of thermalization losses while maintaining or enhancing the spectral range of light which is absorbed. In this work, multijunction LSCs are modeled and simulated using a ray-tracing Monte Carlo model. Two LSC layers are stacked, the top containing CdSe/CdS quantum dots and the bottom containing Si quantum dots. The effects of luminophore concentration on device performance is explored, and photoluminescent coupling effects are examined. The performance of the present multijunction system is then compared with other multijunction LSCs in the literature.

3.1 Monte Carlo Algorithm Modifications

The Monte Carlo algorithm presented in Section 2.2 forms the basis of the simulations used for multijunction LSCs. This algorithm is modified to include the geometry of two LSC layers, as well as the optical properties of the luminophores in both layers. Photons with wavelengths between 400–1100 nm are again injected above the top surface of the top LSC. As photons propagate through the two-layer system, they can interact with either layers; they can be reflected and refracted, absorbed and emitted, and finally, collected by collection mechanisms in either layer. The number photons collected

by each layer, and the collection mechanism within that layer, are explicitly tracked. The result of the simulations is a set of data which could be sorted by incident wavelength, collection layer, and collection mechanism. A diagram of the multijunction system can be seen in Figure 3.1.

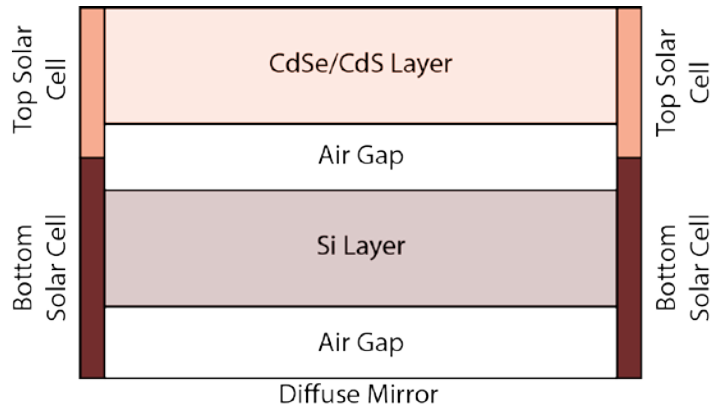


Figure 3.1 A multijunction system with two layers is presented. The top layer contains CdSe/CdS quantum dots; the bottom layer contains Si quantum dots. Each layer has separate collection mechanisms, and light can be collected by separate top or bottom layer solar cells. A diffuse mirror is added beneath the bottom surface of the LSC. Air gaps are added between the two LSC layers and the diffuse mirror.

In addition to data on aggregate photon collection, photons which are absorbed and subsequently emitted are tagged according to which layer they were emitted from. The collection layer and collection mechanism of light emitted from one layer or another can be monitored. Note, the photons are tagged according to which layer they were first emitted from. Photons emitted from one layer and then absorbed and emitted by the other layer are counted in the set of photons emitted from the first layer they were emitted from but not the other. This tracking is used to study photoluminescent coupling, where light emitted from one concentrator interacts with another concentrator.

3.2 Light Absorption in Multijunction LSCs

An analytical model is developed to predict the absorption of light in each layer of the two-layer multijunction LSC. This model can be used to quickly calculate the light absorbed by the top and bottom layers at each wavelength using the absorption spectrum of the luminophores, the optical density of each layer at 450 nm (as a measure of luminophore concentration), and the refractive index of the host polymer. Calculations are used to verify the Monte Carlo model after modifications to simulate the multijunction architecture.

In the analytical model, the multijunction LSC system is treated as a pair of Fabry-Perot etalons, which are transparent or absorbing plates, in this case absorbing, with reflective surfaces at either side. The intensity of light absorbed, reflected and transmitted through these etalons can be calculated [70]. In this treatment, light incident onto a luminescent layer is divided into an infinite series of partial waves whose sums represent the intensity of light transmitted, absorbed and reflected by the layer, respectively. By applying this analysis repeatedly as light propagates through the system, a complete account of the incident light can be given.

3.2.1 First Pass through the Top LSC Layer

Light incident on the top LSC layer is split into an infinite series of partial waves, as shown in Figure 3.2. Light can be reflected, transmitted, or absorbed. The amplitude of partial reflectance, ρ_i , and transmittance, τ_i , waves are

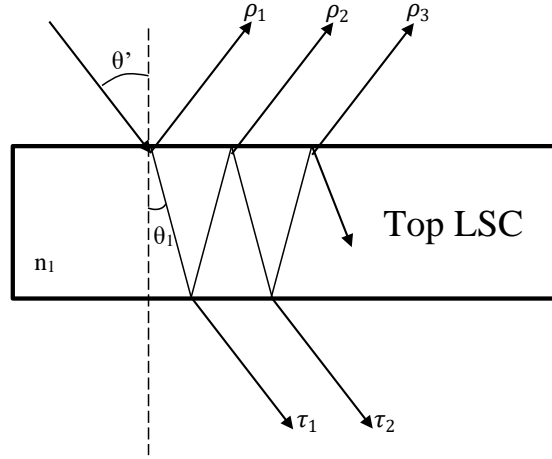


Figure 3.2 Light is incident on the top LSC layer. As the light interacts with the interfaces at the top and bottom of the layer, partial waves form, the sum of which represent the intensity of light reflected, transmitted, and absorbed. Transmitted light is then incident upon the bottom LSC layer.

$$\rho_1 = r , \quad \rho_2 = tt'r'Ae^{i\delta} , \quad \rho_3 = tt'r'^3A^2e^{2i\delta} , \quad \dots \quad (3.1)$$

$$\tau_1 = tt'A^{\frac{1}{2}} , \quad \tau_2 = tt'r'A^{\frac{3}{2}}e^{i\delta} , \quad \tau_3 = tt'r'^2A^{\frac{5}{2}}e^{2i\delta} , \quad \dots \quad (3.2)$$

where r and r' are the reflectivity coefficients for light entering and leaving the LSC, respectively, t and t' are the transmissivity coefficients for light entering and leaving the LSC, respectively, A is the fraction of light *not* absorbed per two passes, and δ is a phase factor given by

$$\delta = \frac{4\pi n_1 l \cos\theta_1}{\lambda} \quad (3.3)$$

where n is the index of refraction of the LSC, l is the thickness of the LSC, θ_1 is the angle of light propagation in the LSC relative to the normal and λ is the wavelength of light.

Notice the reflectivity and transmissivity coefficients are defined such that $R = r^2$ with $r' = -r = -R^{\frac{1}{2}}$ and $t = tt'$, where R is reflectivity and $T = 1 - R$ is transmissivity.

The total amplitude of reflected light, ρ , is the sum of all partial reflected waves. With some simple algebraic manipulation ρ can be represented as the sum of a geometric series.

$$\begin{aligned}\rho &= \rho_1 + \rho_2 + \rho_3 + \dots = R^{\frac{1}{2}} - TR^{\frac{1}{2}}Ae^{i\delta} - TR^{\frac{3}{2}}A^2e^{2i\delta} - TR^{\frac{5}{2}}A^3e^{3i\delta} - \dots \quad (3.4) \\ &= R^{\frac{1}{2}}\left[1 - TAe^{i\delta}(1 + RAe^{i\delta} + R^2A^2e^{2i\delta} + \dots)\right] = R^{\frac{1}{2}}\left(1 - \frac{TAe^{i\delta}}{1-RAe^{i\delta}}\right)\end{aligned}$$

Here we used a simple geometric series formula valid for any $|x| < 1$, namely

$$1 + x + x^2 + \dots = \frac{1}{1-x} \quad (3.5)$$

The intensity of light reflected, I_{rT} , (the subscript T denotes the top LSC layer) by the LSC is equal to the product of the total amplitude of reflected light and its complex conjugate. Shown below is the equation for I_{rT} .

$$\begin{aligned}I_{rT} &= \rho\rho^* = R\left(1 - \frac{TAe^{i\delta}}{1-RAe^{i\delta}}\right)\left(1 - \frac{TAe^{-i\delta}}{1-RAe^{-i\delta}}\right) \quad (3.6) \\ &= R\left[\frac{1 - (R+T)Ae^{i\delta}}{1 - RAe^{i\delta}}\right]\left[\frac{1 - (R+T)Ae^{-i\delta}}{1 - RAe^{-i\delta}}\right] \\ &= R\left(\frac{1 - Ae^{i\delta}}{1 - RAe^{i\delta}}\right)\left(\frac{1 - Ae^{-i\delta}}{1 - RAe^{-i\delta}}\right) \\ &= R\left[\frac{1 + A^2 - A(e^{i\delta} + e^{-i\delta})}{1 + R^2A^2 - RA(e^{i\delta} + e^{-i\delta})}\right]\end{aligned}$$

$$\begin{aligned}
&= R \left[\frac{1 + A^2 - 2A \cos(\delta)}{1 + R^2 A^2 - 2RA \cos(\delta)} \right] \\
&= R \left[\frac{(1 - A)^2 + 2A(1 - \cos(\delta))}{(1 - RA)^2 + 2RA(1 - \cos(\delta))} \right] \\
&= R \left[\frac{(1 - A)^2 + 4A \sin^2\left(\frac{\delta}{2}\right)}{(1 - RA)^2 + 4RA \sin^2\left(\frac{\delta}{2}\right)} \right]
\end{aligned}$$

This procedure can be done to obtain the intensity of light transmitted, I_{tT} as well. The intensity of light absorbed, I_{aT} , is then the difference between unity and the intensities of light reflected and transmitted. The results of those procedures are shown below.

$$I_{tT} = \frac{(1-R)^2 A}{(1-RA)^2 + 4RA \sin^2\left(\frac{\delta}{2}\right)} \quad (3.7)$$

$$I_{aT} = 1 - I_{rT} - I_{tT} \quad (3.8)$$

3.2.2 All Subsequent Passes Before the Mirror

In this section we will analyze all light transmitted through the top LSC in Section 3.2.1. The results of this section will be four equations representing the fractions of light which reaches the mirror (to be analyzed in Section 3.2.3), is absorbed by the top LSC layer, is absorbed by the bottom LSC layer, and is transmitted back out the top of the multijunction LSC, respectively.

In Section 3.2.1 we determined the intensity of light transmitted through the top LSC on the first pass, I_t . This light will reach the bottom LSC, where, as with the top LSC, it will be partially reflected, I'_{rB1} , transmitted, I'_{tB1} , and absorbed, I'_{aB1} . Light reflected from the bottom LSC then reaches the top LSC, where it can be reflected, I'_{rT1} , transmitted,

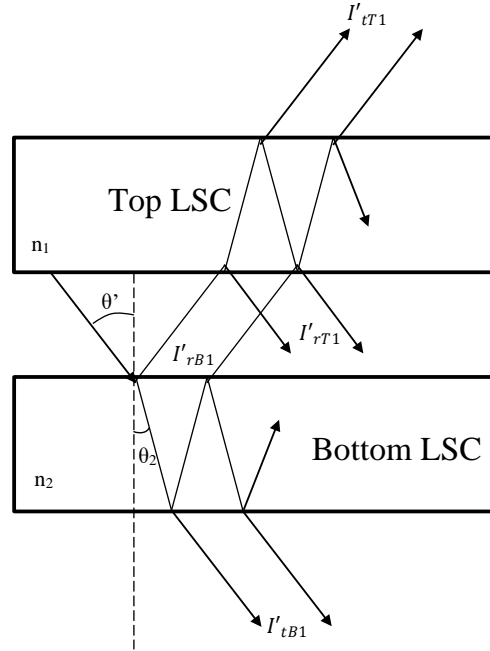


Figure 3.3 Light transmitted through the top LSC layer is incident upon the bottom LSC layer. This light can be reflected back to the top layer, where it can be transmitted or absorbed, it can be absorbed by the bottom layer, or it can be transmitted through the bottom layer, where it is incident upon the diffuse bottom mirror.

I'_{tT1} , or absorbed, I'_{aT1} . Reflected light will then reach the bottom LSC again. An infinite series of reflections will occur, creating an infinite series of intensities such as shown below.

$$I'_{tB1} = I_{tT}I_{tB} , I'_{tB2} = I_{tT}I_{rT}I_{tB}I_{rB} , I'_{tB3} = I_{tT}I_{rT}^2I_{tB}I_{rB}^2 , \dots \quad (3.9)$$

$$I'_{aB1} = I_{tT}I_{aB} , I'_{aB2} = I_{tT}I_{rT}I_{rB}I_{aB} , I'_{aB3} = I_{tT}I_{rT}^2I_{rB}^2I_{aB} , \dots \quad (3.10)$$

$$I'_{tT1} = I_{tT}^2I_{rB} , I'_{tT2} = I_{tT}^2I_{rT}I_{rB}^2 , I'_{tT3} = I_{tT}^2I_{rT}^2I_{rB}^3 , \dots \quad (3.11)$$

$$I'_{aT1} = I_{tT}I_{aT}I_{rB} , I'_{aT2} = I_{tT}I_{aT}I_{rT}I_{rB}^2 , I'_{aT3} = I_{tT}I_{aT}I_{rT}^2I_{rB}^3 , \dots \quad (3.12)$$

As in Section 3.2.1, the sum of these infinite sets of terms form the total intensity of light transmitted through the bottom, absorbed in the bottom, transmitted through the top and absorbed in the top, respectively. The terms form a geometric series, the sum of which can be simplified using the equation for a geometric series presented in Section 3.2.1. This leads to the following equations.

$$I'_{tB} = \frac{I_{tT}I_{tB}}{1-I_{rT}I_{rB}} \quad (3.13)$$

$$I'_{aB} = \frac{I_{tT}I_{aB}}{1-I_{rT}I_{rB}} \quad (3.14)$$

$$I'_{tT} = \frac{I_{tT}^2 I_{rB}}{1-I_{rT}I_{rB}} \quad (3.15)$$

$$I'_{aT} = \frac{I_{tT}I_{aT}I_{rB}}{1-I_{rT}I_{rB}} \quad (3.16)$$

3.2.3 First Set of Reflection Off Mirror

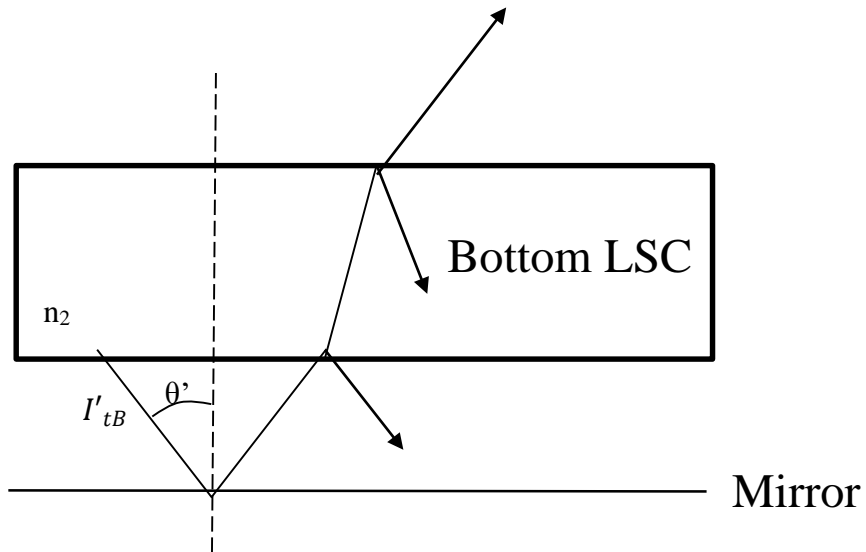


Figure 3.4 Once light pass through the bottom LSC layer it reaches the mirror and is reflected back towards the bottom layer, where it can be absorbed or transmitted.

Light passing through to the mirror will be reflected off the mirror and transmitted, reflected or absorbed by the bottom LSC. However, any reflected light is not lost. Rather, it is reflected again off the mirror and returns to the bottom LSC. Throughout the course of an infinite number of reflections, all light will be either absorbed or transmitted through the bottom LSC. Then the intensity of light transmitted is the product of the intensity of incident light and the ratio of transmitted light to the sum of transmitted and absorbed light. The intensity of light transmitted and absorbed by the bottom LSC (with I'_{tB} the intensity of incident light, as derived in Section 3.2.2) are given by I''_{tB1} and I''_{aB1} , respectively. The parameters x_t and x_a are introduced here to condense future equations.

$$I''_{tB1,1} = \frac{I'_{tB}I_{tB}}{I_{tB}+I_{aB}} = I'_{tB}x_t \quad (3.17)$$

$$I''_{aB1,1} = \frac{I'_{tB}I_{aB}}{I_{tB}+I_{aB}} = I'_{tB}x_a \quad (3.18)$$

3.2.4 All Reflection Off Mirror

In Section 3.2.1 we derived an equation for light reflected off the mirror and transmitted through the bottom LSC layer. This light will then be incident on the top LSC layer. Notice this is analogous to the system treated in Section 3.2.1. Therefore, we can use the equations derived in that section (with a different intensity of incident light, of course). Note, in Section 3.2.2 light was incident on the bottom LSC layer. In the present case, light is incident on the top LSC layer. These equations represent the light transmitted through the top and bottom LSC layers, and absorbed through the top and bottom LSC layers.

$$I''_{tB2,1} = \frac{I''_{tB1,1}I_{rT}I_{tB}}{1-I_{rT}I_{rB}} = I''_{tB1,1}Y_t \quad (3.19)$$

$$I''_{aB2,1} = \frac{I''_{tB1,1}I_{rT}I_{aB}}{1-I_{rT}I_{rB}} = I''_{tB1,1}Y_a \quad (3.20)$$

$$I''_{tT1} = \frac{I''_{tB1,1}I_{tT}}{1-I_{rT}I_{rB}} = I''_{tB1,1}Z_t \quad (3.21)$$

$$I''_{aT1} = \frac{I''_{tB1,1}I_{aT}}{1-I_{rT}I_{rB}} = I''_{tB1,1}Z_a \quad (3.22)$$

Light transmitted through the bottom LSC, $I''_{tB2,1}$, will be incident on the mirror and an analysis analogous to the one in Section 3.2.3 can be performed. This leads to an infinite series, resulting in the following equations,

$$I''_{tB1,1} = I''_{tB}x_t , \quad I''_{tB1,2} = I''_{tB2,1}x_t , \quad I''_{tB1,3} = I''_{tB2,2}x_t , \quad \dots \quad (3.23)$$

$$I''_{aB1,1} = I''_{tB}x_a , \quad I''_{aB1,2} = I''_{tB2,1}x_a , \quad I''_{aB1,3} = I''_{tB2,2}x_a , \quad \dots \quad (3.24)$$

$$I''_{tB2,1} = I''_{tB1,1}y_t , \quad I''_{tB2,2} = I''_{tB1,2}y_t , \quad I''_{tB2,3} = I''_{tB1,3}y_t , \quad \dots \quad (3.25)$$

$$I''_{aB2,1} = I''_{tB1,1}y_a , \quad I''_{aB2,2} = I''_{tB1,2}y_a , \quad I''_{aB2,3} = I''_{tB1,3}y_a , \quad \dots \quad (3.26)$$

$$I''_{tT1} = I''_{tB1,1}z_t , \quad I''_{tT2} = I''_{tB1,2}z_t , \quad I''_{tT3} = I''_{tB1,3}z_t , \quad \dots \quad (3.27)$$

$$I''_{aT1} = I''_{tB1,1}z_a , \quad I''_{aT2} = I''_{tB1,2}z_a , \quad I''_{aT3} = I''_{tB1,3}z_a , \quad \dots \quad (3.28)$$

Let's look specifically at the light absorbed by the bottom LSC, given by the equation below.

$$I''_{aB} = \sum_{i=1}^{\infty} I''_{aB1,i} + I''_{aB2,i} \quad (3.29)$$

Notice the series is iterative, as shown below. When simplified, the terms form two geometric series, which yield a final equation for the absorption of light in the bottom LSC.

$$\begin{aligned}
I''_{aB} &= I''_{aB1,1} + I''_{aB1,2} + I''_{aB1,3} + \dots \\
&+ I''_{aB2,1} + I''_{aB2,2} + I''_{aB2,3} + \dots \\
&= I'_{tB}x_a + I''_{tB2,1}x_a + I''_{tB2,2}x_a + \dots \\
&+ I''_{tB1,1}y_a + I''_{tB1,2}y_a + I''_{tB1,3}y_a + \dots \\
&= I'_{tB}x_a + I''_{tB1,1}y_t x_a + I''_{tB1,2}y_t x_a + \dots \\
&+ I'_{tB}x_t y_a + I''_{tB2,1}x_t y_t + I''_{tB2,2}x_t y_t + \dots \\
&\dots \\
&= I'_{tB}x_a + I'_{tB}y_t x_a^2 + I'_{tB}y_t^2 x_a^3 + \dots \\
&+ I'_{tB}x_t y_a + I'_{tB}x_t^2 y_a y_t + I'_{tB}x_t^3 y_a y_t^2 + \dots \\
&= I'_{tB} \left(\frac{x_a}{1 - x_t y_t} + \frac{x_t y_a}{1 - x_t y_t} \right) \\
&= I'_{tB} \left(\frac{x_a + x_t y_a}{1 - x_t y_t} \right)
\end{aligned} \tag{3.30}$$

A similar analysis can be performed to determine the intensity of light absorbed by the top LSC layer and transmitted through the top LSC layer. Equations for these values are given below.

$$I''_{aT} = I'_{tB} \left(\frac{x_t z_a}{1 - x_t y_t} \right) \tag{3.31}$$

$$I''_{tT} = I'_{tB} \left(\frac{x_t z_t}{1 - x_t y_t} \right) \tag{3.32}$$

3.2.5 Total Absorption and Losses

In the previous three sections, we analyzed light as it passed through a multi-junction LSC. In this section we'll put it all together. In all, light can be absorbed by the top LSC layer, absorbed by the bottom LSC layer, or lost out the top of the multi-junction LSC. The intensity light absorbed or lost is simply the sum of the intensities found in the preceding sections, respectively. Thus,

$$I_{aT}^{total} = I_{aT} + I'_{aT} + I''_{aT} \quad (3.33)$$

$$I_{aB}^{total} = I_{aB} + I'_{aB} + I''_{aB} \quad (3.34)$$

$$I_{tT}^{total} = I_{tT} + I'_{tT} + I''_{tT} \quad (3.35)$$

3.2.6 Model Results and Monte Carlo Model Comparison

The absorption of light by each layer is calculated using this model, with no top or bottom mirrors present, but perfect specular mirrors placed on the sides. Results from the

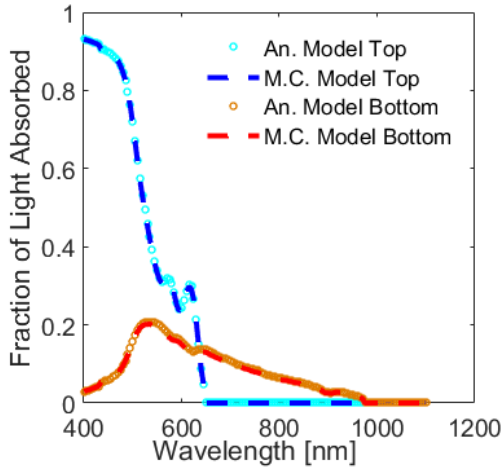


Figure 3.5 The fraction of incident light absorbed calculated from the analytical model (dotted) is compared to Monte Carlo simulations (dashed). Top layer absorption is given in blue, while bottom layer absorption is shown in red.

analytical calculations and Monte Carlo simulations are shown in Figure 3.5.

The simulations show excellent agreement with the analytical model calculations. The relative percent difference is within 1% for the top layer and 5% for the bottom layer, with the Monte Carlo simulations displaying slightly lower absorption values. These results verify the accuracy of the multijunction model and provide confidence for future simulations.

3.3 Multijunction LSC Simulations

Monte Carlo simulations are used to study the multijunction system. Two layers, each with lateral size 1 m x 1 m, are stacked with a 1 mm air gap separating them. The top layer contains CdSe/CdS quantum dots with quantum yield 75%, while the second layer contains Si quantum dots with quantum yield 50%. These quantum yields are chosen to reflect experimentally realizable values. PMMA is selected as the host polymer in both layers. The absorption and emission spectra for each luminophore is taken from experimental measurements.

3.3.1 Optical Density

The optical density, or concentration, of luminophores is an important parameter in any LSC. Light absorption and reabsorption losses are greatly affected by the concentration of luminophores in the concentrator, so optimizing this parameter is required for maximum performance. The multijunction model is used here to determine the optimum optical density of each layer of the multijunction LSC.

There are two competing factors associated with luminophore concentration: increasing optical density increases absorption, but also allows more emitted light to be

reabsorbed [71]. This tradeoff is further complicated for multijunction systems by the presence of different luminophores. In a single layer LSC absorption of all light with energy above the band gap is desired, but in a multijunction LSC each layer should absorb a different spectral range. Specifically, the top layer should absorb light above the band gap, while the bottom layer should absorb light between the band gaps of the top and bottom layer luminophore.

As a first step to finding the optimal optical density, and to demonstrate the tradeoff between light absorption and reabsorption losses, bottom layer optical density is varied while holding top layer OD = 1.0 at 450 nm. An optimum bottom layer optical density is observed at 0.2 at 450 nm, as seen in Figure 3.6, which shows the fraction of light reaching the bottom layer solar cell at varying wavelength and bottom layer optical density.

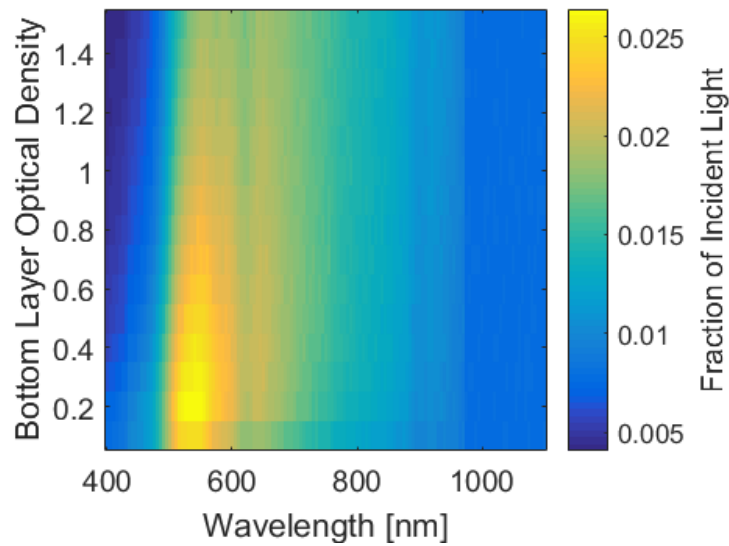


Figure 3.6 The bottom layer optical density at 450 nm was varied from 0.1 to 1.5. The fraction of incident light reaching the edge of the bottom layer concentrator is plotted against bottom layer optical density at 450 nm and wavelength.

To observe the competing factors, absorption and reabsorption are tracked explicitly. The total number of photons absorbed by the bottom layer is found to increase monotonically with optical density. However, of the light absorbed and emitted by the bottom layer, the fraction lost to reabsorption losses in the bottom layer also increases monotonically. This means that although more light is absorbed at higher optical density, less of the absorbed light reaches the edge of the concentrator. Figure 3.7 shows bottom layer light absorption and the fraction of absorbed light reaching the edge. These observations demonstrate how increasing bottom layer optical density increases both light absorption and reabsorption losses, creating the optimum observed.

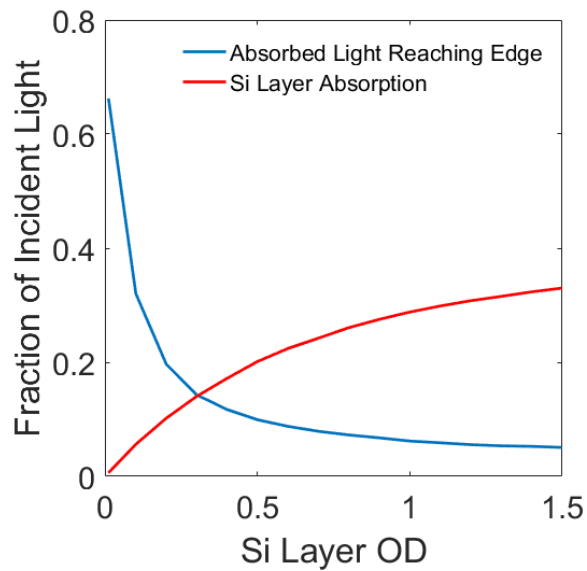


Figure 3.7 As bottom layer optical density increases, the fraction of incident light absorbed by the bottom layer (red) increases. However, due to reabsorption losses, the fraction of absorbed light which reaches the edge of the bottom layer concentrator (blue) decreases.

An optimum bottom layer optical density of 0.2 at 450 nm is found assuming a top layer optical density of 1 at 450 nm. By allowing the optical density of both layers to

change, an interdependence of layer performance is observed. Namely, the performance of the bottom layer is dependent on light absorption in the top layer.

An iterative method is used to find the optimum optical density of each layer. The first iteration was discussed previously: the optical density of the top layer was fixed at 1 while the optimum bottom layer optical density was determined. Then, the bottom layer optical density is fixed at this optimum, 0.2, while top layer optical density is optimized. Luminophore concentration in the bottom layer is then varied again, this time holding the top layer optical density at the new value. This process is continued until an optimum set of values is found to within 0.01 at 450 nm. Multijunction LSC performance in this system is optimized at optical densities of 0.15 for the top layer and 0.07 for the bottom layer.

A shift in optimal bottom layer optical density is observed, from 0.2 to 0.07, as top layer optical density decreases from 1 to its optimum value, 0.15. When the concentration of luminophores in the top layer is decreased, top layer absorption decreases. This leads to an increase in bottom layer absorption, as more light is transmitted through the top layer and is incident upon the bottom layer. The change in bottom layer absorption due to top layer concentration alters the balance point, the optimum, between light absorption and reabsorption losses in the bottom layer. This balance is pushed to lower optical densities, where light absorption can remain relatively high while decreasing reabsorption losses.

The performance of the optimal concentrator system is shown in Figure 3.8. At wavelengths shorter than about 500 nm, the top layer collects more light than the bottom due to strong absorption at these wavelengths and higher quantum yield. However, the top concentrator does not absorb past 650 nm, so little light is guided to the edge for

wavelengths longer than 650 nm. In contrast, the bottom layer concentrator absorbs throughout the visible and into the near-IR. Therefore, the bottom layer experiences a more gradual decrease in efficiency as wavelength lengthens. When weighted over the solar spectrum between 400 nm and 1100 nm, the bounds of the present simulations, the top layer has an optical efficiency of 3.02% and the bottom layer has an optical efficiency of 2.20%. The overall optical efficiency of the multijunction LSC is 5.22%.

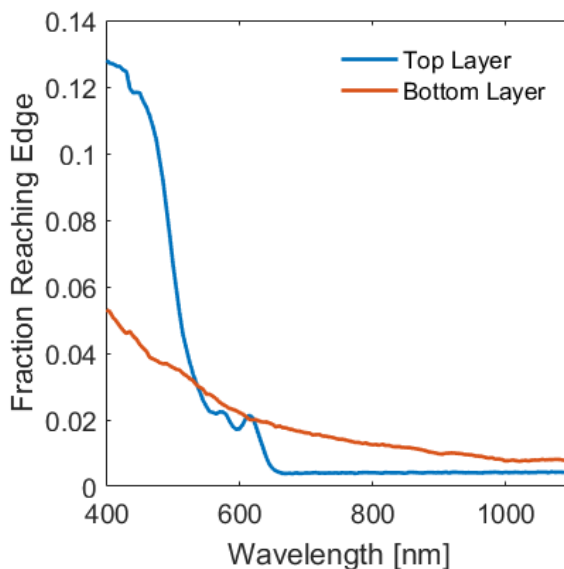


Figure 3.8 The fraction of incident light reaching the edge of the top layer (blue) and bottom layer (red) concentrators is shown. At short wavelengths, the top layer efficiently collects and guides light, though it collects little light at wavelengths longer than 650 nm.

3.3.2 Photoluminescent Coupling Effects

The dependence of bottom layer design and performance upon top layer design was discussed in the previous section. In this section another type of layer interdependence is explored: photoluminescent coupling. Light absorbed and emitted in one layer may propagate into the other layer and interact with luminophores there, leading to the

interdependence of top and bottom layer performance. These effects can give rise to nonlinear behavior in multijunction system efficiency, whereas improvement in the efficiency of one layer can also improve performance in the other layer. The extent of these coupling effects in the present multijunction LSC system is studied to gain insights into LSC layer interdependence. Emitted photons are sorted by which layer they were emitted from. The collection mechanisms for photons absorbed and emitted from each layer are tracked separately, allowing for an explicit examination of how emission from one layer affects the performance of the other layer.

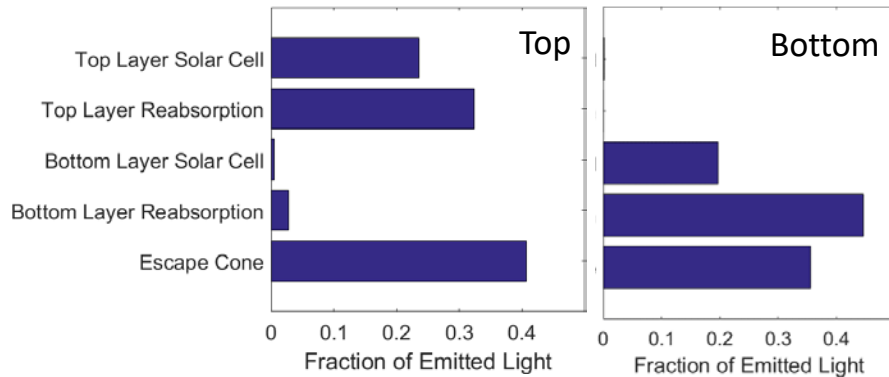


Figure 3.9 Photons emitted by the top (left) and bottom (right) layers are separated, and their collection mechanisms are tracked. A majority of emitted photons are lost to the escape cone or collected within the same layer they were emitted from.

From Figure 3.9, it is seen that the effects of coupling are relatively small in the present system. Virtually no light emitted by the bottom layer was collected by the top layer solar cell or lost to top layer reabsorption. Therefore, the presence of the bottom layer does not increase top layer efficiency through photoluminescent coupling effects. The reason for this lack of coupling can be explained by observing in Figure 1.3 that there is

little overlap between the top layer absorption spectrum and bottom layer emission spectrum.

While there is little overlap between top layer absorption and bottom layer emission, there does exist significant overlap between the bottom layer absorption spectrum and top layer emission spectrum, leading to coupling. The presence of coupling effects is evident in top layer-emitted light, where 3.82% of light emitted by the top layer was reabsorbed by the bottom layer. Although coupling is observed in the present system, the performance increase of the bottom layer due to this coupling is slight.

Despite the lack of efficiency gain due to photoluminescent coupling in the present system, it should be noted that this multijunction system does not contain a mirror above the surface of the top layer. As a result, trapping is relatively poor in these concentrators, leading to few opportunities for light emitted from one layer to interact with the other. If a top mirror was added to the concentrator, light could be trapped between the top and bottom mirrors, passing several times through each of the layers, giving rise to many opportunities for interactions. Photoluminescent coupling is expected to be much more prominent in these cases.

3.3.3 Ideal Top Mirrors

Wavelength-selective mirrors placed above the top surface of a single layer LSC serve to transmit high energy light into the concentrator while trapping emitted light, maintain high light absorption while reducing escape cone losses. These mirrors offer the same potential for multijunction LSCs. Designing a wavelength-selective mirror for a stacked concentrator system has added complexity due to the presence of two absorption

bands and two emission bands (one for each layer). Simulations are performed placing idealized top mirrors above the multijunction LSC to evaluate the potential of these mirrors for efficiency improvement.

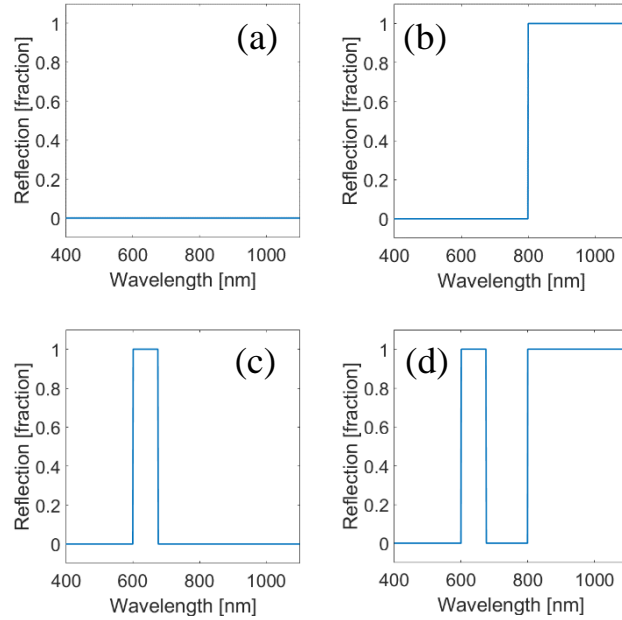


Figure 3.10 Four multijunction LSCs were examined with various top mirrors. (a) No top mirror is added. (b) A top mirror is added above the surface of the top LSC layer. This mirror has a reflection band from 800 nm to 1100 nm, overlapping with the emission spectrum of Si quantum dots. (c) This mirror has reflection from 600 nm to 675 nm, overlapping with the emission spectrum of CdSe/CdS quantum dots. (d) The final mirror has reflection bands from 600 nm to 675 nm and from 800 nm to 1100 nm.

Before designing photonic mirrors, as was done in Section 2.1, idealized cases are examined to determine the desired reflection band of the top mirror and the performance enhancement potential of top mirrors for a multijunction configuration. Simulations are performed on four multijunction LSC systems: no top mirror (Figure 3.10(a)), a mirror whose reflection band overlaps with the emission spectrum of Si quantum dots (Figure

3.10(b)), a mirror whose reflection band overlaps with the emission spectrum of CdSe/CdS quantum dots (Figure 3.10(c)), and finally, a mirror with reflection bands which overlap with the emission spectra of both luminophores (Figure 3.10(d)). For each of the idealized top mirrors, reflectivity is one within the reflection band, and zero outside of it. The reflection bands do not blue shift with angle of incidence.

An increase in the fraction of light reaching the edge of the concentrators is observed for wavelengths outside the reflection band of the mirrors due to the enhanced trapping provided by the mirrors. However, no light within the reflection band is collected as all light within the reflection band is reflected. Edge collection from both layers is given in Figure 3.11.

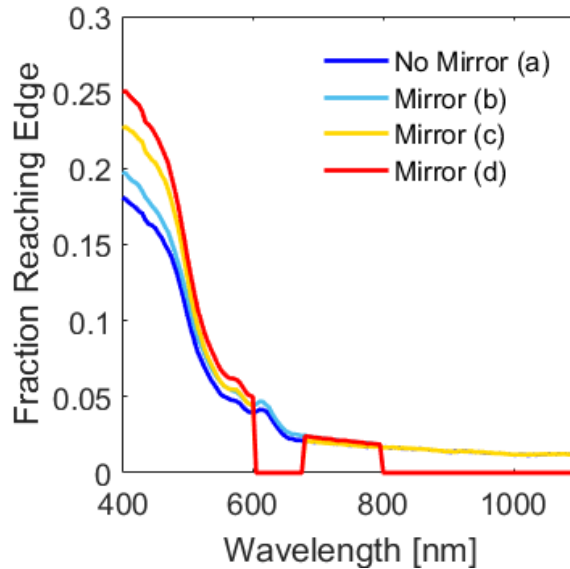


Figure 3.11 The fraction of light reaching the concentrator edge is compared for an open top system, and the three idealized mirrors (see Figure 3.10). The sum of light reaching the top layer edge and light reaching the bottom layer edge is given.

The performance of these three idealized cases are compared. For the multijunction LSC with no top mirror, 5.22% of light is collected at the edge, weighting by the solar spectrum from 400 nm to 1100 nm. Upon the addition of the first mirror (Figure 3.10(a)) there is little change in performance as 5.31% of light reaches the edge. Although the presence of the mirror reduces escape cone losses, there is also an increase in reabsorption as photons trapped between the mirrors pass several times through the concentrators. Increased reabsorption and reflection losses reduce the effectiveness of this mirror at boosting efficiency. The second mirror (Figure 3.10(b)) has an optical efficiency of 5.76%, a relative increase of 10% from the open top system. Reabsorption and reflection losses also increase upon the addition of this mirror. However, the mirror is much more effective at reducing escape cone losses, with less than half the escape cone losses of the first mirror system. The third mirror is a combination of the first two, and increases efficiency to 5.92%, a relative increase of 13%. Escape cone losses in this system constitute less than 1% of incident light for a multijunction system with this mirror.

Three idealized top mirrors are added above the top surface of the multijunction LSC to evaluate the potential benefits from such mirrors. Moderate gains in efficiency are observed, with efficiency improvements up to 13%. The width and wavelength range of the reflection bands of these mirrors are not varied, and it is likely that further increases could be seen with optimization. However, much of the performance gains provided by these top mirrors may be damped as idealities are relaxed. Imperfect reflection within the reflection band and imperfect transmission outside the reflection band may lead to decreases in the performance enhancing effects of the mirrors.

3.4 Multijunction LSC Performance

In this section a multijunction LSC with two layers is examined. The top layer contains CdSe/CdS quantum dots with quantum yield 75% and an optimum optical density of 0.15 at 450 nm. The bottom LSC layer contains Si quantum dots with quantum yield 50% and optimum optical density 0.07 at 450 nm. Each of the layers is 1 m x 1 m in lateral size and 0.003 m thick. A diffuse mirror is placed beneath the bottom surface of the LSC to increase light absorption and trapping. The fraction of light reaching the edge of each layer is determined for a wavelength range of 400 nm to 1100 nm. When weighting by the solar spectrum within that range, an optical efficiency of 3.02% for the top layer and 2.20% for the bottom layer is found, for an overall optical efficiency of 5.22%.

The efficiency of other multijunction LSCs reported in the literature is given in Table 3.1. While it is difficult to compare results directly due to differences in LSC size and efficiency measurement methodology, some works report optical efficiency while other measure the PCE of edge-mounted solar cells, the efficiency of the concentrator in this work is similar to reported literature values. Optical efficiency is known to decrease with concentrator size, so the large lateral sizes used in present simulations lead to lower efficiency than many of the smaller concentrators in the literature. Conversely, the presence of a diffuse back mirror, absent in other works, boosts efficiency.

Table 3.1 Efficiencies for multijunction LSCs in the literature are reported. The type of luminophore, concentrator size, efficiency, and efficiency type (PCE or optical efficiency) is given, along with corresponding references.

Luminophores	Size (cm ³)	Efficiency	Efficiency Type	Ref.
BA241 Dye BA856 Dye	2 x 2 x 0.3	6.7%	PCE	[55]
C-dots CdPb(Br _{0.8} Cl _{0.2}) ₃ CsPb(Br _{0.2} I _{0.8}) ₃	10 x 10 x 0.2	3.05%	PCE	[72]
Mn: Cd _x Zn _{1-x} S/ZnS CuInSe ₂ /ZnS	15.24 x 15.24 x 0.16	6.4%	Optical	[29]
Three Dyes	120 x 13.5 x 0.2	6.1%	Optical	[73]
DCJT B Dye Pt(TPBP)	2.5 x 2.5 x 0.2	6.8%	PCE	[74]
Lumogen F Red305 Yellow CRS040	5 x 5 x 0.5	7.1%	PCE	[75]
CdSe/CdS Si	100 x 100 x 0.3	5.22%	Optical	This work

Chapter 4. Thin Film LSC Simulations

Thus far, single junction and multijunction LSC simulations have utilized a bulk polymer architecture, where luminophores are homogeneously dispersed in a polymer medium. Thin film LSCs consist of a film of polymer embedded with luminophores, having a thickness close to the wavelength of emitted light, deposited onto a glass substrate. In this architecture sunlight is absorbed by luminophores in the thin film, which then emit light into the glass substrate where it is guided to the edges via total internal reflection. The thin film architecture may provide performance advantages by allowing fluorescent light to propagate within a lossless glass substrate instead of an absorbing polymer slab. However, the angles of emitted light are also modified by the thin film structure. It is, therefore, critical to understand how light interacts with a thin film LSC and to evaluate the differences between the bulk polymer and thin film architectures. Here, a thin film LSC is modeled. The performance of thin film LSCs is calculated and compared to a bulk polymer concentrator.

4.1 Ray and Wave Optics Model

The simulation of thin film LSCs is more complicated than bulk polymer LSCs as the thickness of the film is close to the wavelengths of incident and emitted light, giving rise to wave effects which cannot be accounted for using a ray-tracing model. These thin film effects alter the angular distribution of emission from the luminophores, reabsorption within the concentrator, and reflection off the top face of the LSC. To model these effects, a wave optics model is required. A 3D FDTD model is developed to calculate the angular distribution of the emission of light from a luminophore within the thin film, as well as

light reabsorption in the film. An analytical model is used to calculate thin film absorption, reflection, and transmission. Data from these calculations is then integrated into a Monte Carlo ray-tracing model which simulates the performance of thin film LSCs.

The Monte Carlo algorithm is similar to the one used in Chapter 2. The geometry of the system is changed, however. Instead of assuming luminophores are homogeneously dispersed within a bulk polymer layer, a glass substrate with an infinitely thin polymer-luminophore film on its top face is modeled. Light incident upon the top face of the LSC can be absorbed by the thin film, reflected, or transmitted, where the probability of absorption, reflection, and transmission is calculated by an analytical model. Absorbed light can then be lost to absorption losses due to non-unity quantum yield, emitted into the air, emitted into the glass substrate, or emitted and reabsorbed without leaving the thin film. The angular distribution of luminescence into the air and substrate, as well as the probability of reabsorption, is determined from the FDTD calculations. Light propagates through the system until it is lost to one of the loss mechanisms discussed in Section 2.2 or reaches the edge of the concentrator. The collection mechanisms in these simulations are almost the same as those of the bulk polymer simulations. However, escape cone losses are split between losses to the air and losses through the substrate.

4.2 Dipole Emission in a Homogeneous Medium and Dielectric Half Space

Before simulating the emissive properties of luminophores in a thin film, the FDTD model is tested using simpler systems. First, a dipole is placed in a 3D homogenous dielectric medium with $n = 1.0$, where it should exhibit isotropic emission. Perfectly matched boundary conditions are used at each boundary of the simulation region. Using

this boundary condition, all light reaching the edge of the simulation is absorbed by the boundary, none of the light is reflected back into the simulation region. Monitors are placed above and beneath the dipole to measure the electric field upon emission. This data is transformed into the far field, where the angular distribution of emission is determined. Dipole orientation is taken as isotropic. Thus, three simulations are run with varying dipole orientations, each orthogonal to the other two, and averaged.

The angular distribution of emission for a dipole in a homogeneous medium is shown in Figure 4.1. In this figure, 0 degrees denotes the direction normal to the bottom monitor (see Figure 4.1 inset), 90 degrees denotes the direction parallel to the monitor surface, and 180 degrees denotes the direction normal to the top monitor. Emission is observed as isotropic at most angles. However, from 70 to 90 degrees, and from 110 to 90 degrees, emission intensity sharply decreases to zero. While isotropic emission is expected at all angles, this decrease to zero emission at 90 degrees is not due to an error in the simulation but a model limitation. The monitors above and beneath the dipole measure emission intensity above and beneath the dipole. However, these monitors cannot measure light emitted parallel or nearly parallel to their surface, that is, light emitted near 90 degrees. As a result, far field calculations are performed assuming no electric field intensity past the edges of the monitor. It is this boundary condition which gives rise to the observed feature.

It is important to note that for all future simulations, the model will not be accurate for some angles near 90 degrees. However, the range of angles over which the model yields inaccurate results, between 70 and 110 degrees in the case of a dipole in a homogeneous medium, will vary depending on the simulation. For instance, for the case of a dipole in a

thin film, which will be discussed in Section 4.3, little light is emitted at angles near 90 degrees. Thus, the zero electric field intensity boundary condition on the monitors is a better assumption than in the homogeneous medium case. Therefore, the model is expected to be accurate for a large range of angles.

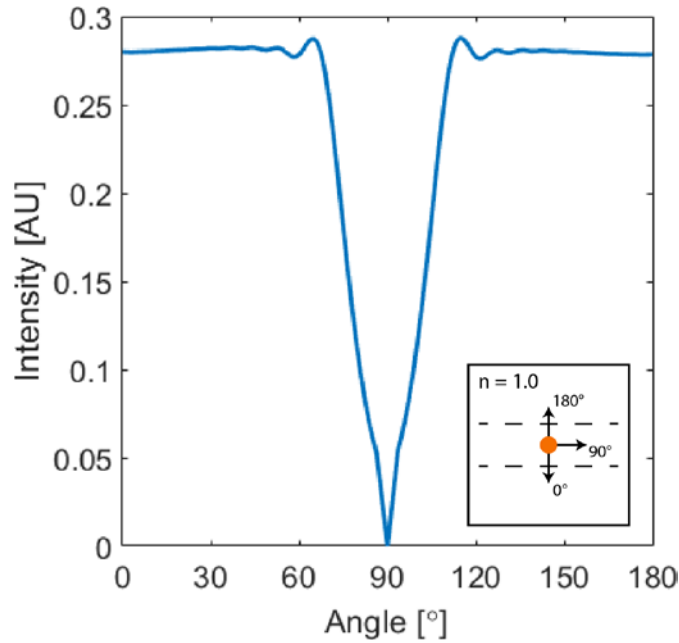


Figure 4.1. The angular distribution of emission from a dipole in a homogeneous medium is shown. Isotropic emission is seen for most angles, but emission intensity falls to zero at 90 degrees. The inset shows the model, where a dipole is placed in an $n = 1.0$ lossless medium. Two monitors (represented by dotted lines) are placed above and beneath the dipole. 0 degrees denotes the direction beneath the dipole, 90 degrees denotes the direction to the side of the dipole, and 180 degrees denote the direction above the dipole.

After studying the homogeneous case to determine the limitations of the FDTD model, a dipole is placed near a dielectric half space to observe how a nearby interface alters dipole emission. A dipole emission wavelength of 645 nm is chosen, which corresponds to the peak emission wavelength of CdSe/CdS quantum dots. Refractive index

data is measured for a thin film with CdSe/CdS core-shell quantum dots and for a glass substrate using spectroscopic ellipsometry, as discussed in Chapter 5. These data are imported into the FDTD model, where the upper region of the half space has the real refractive index of the thin film and the lower region of the half space has the refractive index of glass. Note, the imaginary component of the refractive index is set to zero for half space simulations. At 645 nm, the refractive index of the upper region is 1.60, and the refractive index of the lower region is 1.52.

The dipole is placed in the upper region a height, H , from the interface. This height is varied from 100 nm to 1000 nm. The angular distribution of dipole emission for various heights is given in Figure 4.2. When the dipole is near the interface, a sharp peak in emission intensity forms at steep angles (near 90 degrees) in the upper region. Additionally, more light is emitted into the upper region. This preferential emission into the upper region occurs due to the difference in refractive index. As the dipole moves away from the interface, the emission intensity peak decreases and emission intensity into the lower region increases, moving towards isotropic behavior. While anisotropic emission is still observed at a distance of 1000 nm from the interface, the anisotropic features are significantly less distinct.

Generally, a dipole near a dielectric interface will emit more light into the higher refractive index medium, with a preference for emission at steep angles. This is favorable for our thin film LSCs, as the refractive index of the glass substrate is larger than that of the air, so preferential emission into the substrate is expected. Emission at steep angles is also beneficial as light emitted into the substrate has a more direct path towards the edge.

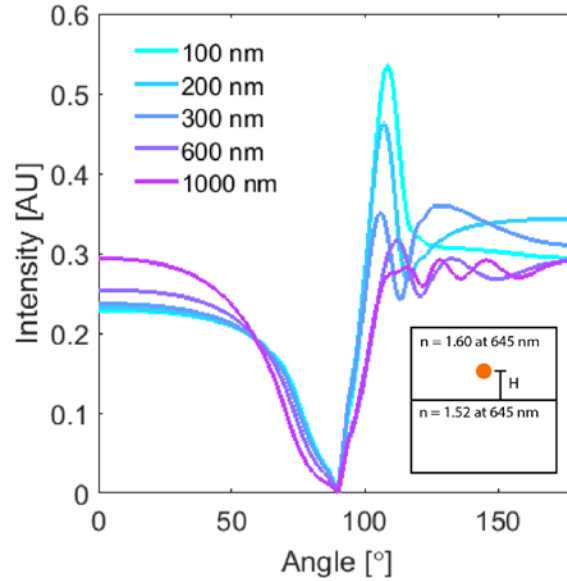


Figure 4.2. A dipole is placed in a dielectric half space at various distances from the interface. The angular distribution shows anisotropic behavior at short heights, trending towards isotropic emission as the dipole is moved away from the interface. The half space model is shown in the inset, where a dipole is placed a distance H away from the interface between two dielectric materials.

4.3 Dipole Emission in a Thin Film

After testing the FDTD model for simpler cases of dipole emission in a homogeneous medium and dipole emission near a dielectric half space, a dipole is placed in a thin film to model the thin film LSC system. Thin film effects on dipole emission and the reabsorption of emitted light are calculated. The thickness of the thin film is varied from 100 nm to 1500 nm to determine how LSC performance can be altered by changing thin film thickness.

4.3.1 Dipole Height and Orientation

In these simulations, air above the thin film and the glass substrate beneath the thin film are treated as semi-infinite layers. Monitors are placed above and beneath the thin

film, parallel to its top and bottom interfaces. The refractive index of the thin film and the substrate are taken from experimental measurements, as discussed in the previous section. Note, for thin film simulations, the imaginary component of the refractive index of the thin film is not set to zero. For each simulation, three cases are run with varying dipole orientations. Figure 4.3 shows the electric field intensity map for emission from a dipole in a 100 nm thick film into the glass substrate for different dipole orientations. In these simulations, the hemispherical distribution of electric field intensity above and beneath the thin film is calculated. This hemisphere is then projected onto a circle, which is what is shown in the figure. Here, the X and Y directions are parallel to the monitors (and the interfaces between the air, thin film, and substrate), while the Z direction is normal to the

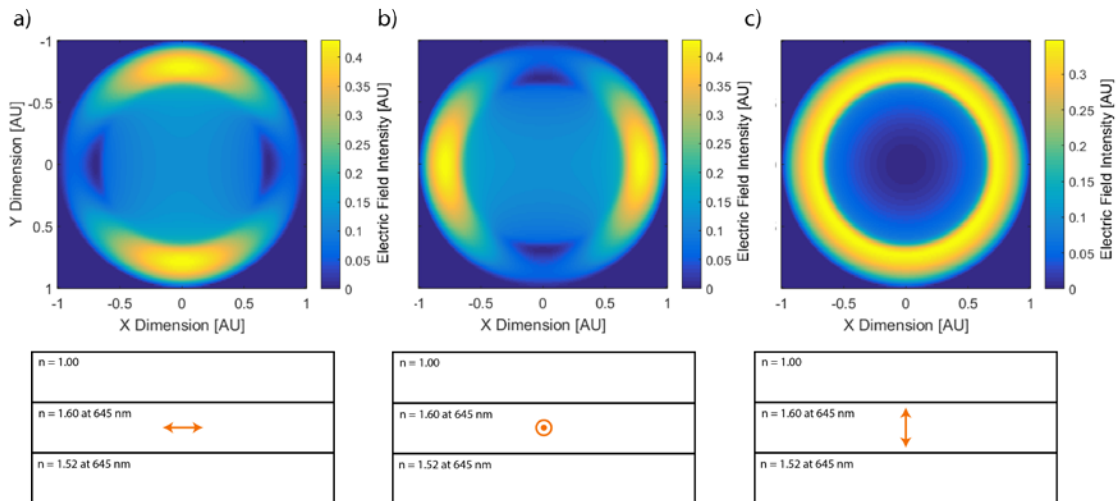


Figure 4.3 Electric field maps are shown for dipoles oriented in the a) X, b) Y, and c) Z directions. The electric field intensity map is a 2D projection of the hemispherical distribution of electric field intensity beneath the thin film, i.e. into the substrate. Note, the outside box of the diagrams beneath the electric field intensity maps denotes the edge of the simulation region. The air and substrate are treated as semi-infinite in height.

monitors. The three dipole orientations are averaged to yield results for an isotropic mixture of dipole orientation, which is a reasonable assumption for luminophores dispersed in a thin polymer film.

In addition to averaging results over dipole orientation, it is also important to consider different dipole heights within the film. As seen in Section 4.2, the angular distribution of emission changes as a dipole is moved closer or farther away from a dielectric interface. Similarly, the angular distribution of emission will change as the dipole is moved closer to the air/thin film interface or the thin film/substrate interface. Figure 4.4 shows the angular distribution for a 700 nm thin film at (a) varying dipole heights, and (b) the average angular distribution. At different heights the angular distribution changes, with

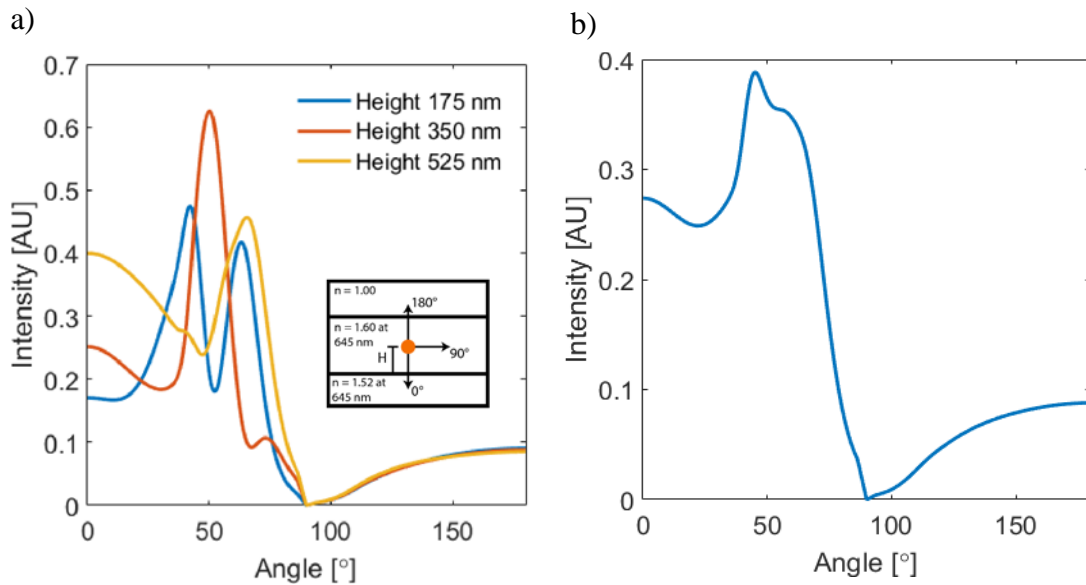


Figure 4.4 The angular distribution of emission from a dipole in a 700 nm thin film is given. The height of the dipole within the thin film was varied, placing the dipole 1/4, 1/2, and 3/4 of the film thickness away from the thin film/substrate interface (a). The three angular distributions were averaged to yield the average angular distribution of emission from a dipole in a 700 nm thin film (b). Note, the outside box in the inset denotes the edge of the simulation region. The air and substrate are treated as semi-infinite in height.

variation in the maximum angle, the intensity, and the number of angle maxima. No one height captures the shape of the average angular distribution. Therefore, for all subsequent simulations nine simulations are averaged, with the dipole placed $T/4$, $T/2$, and $3T/4$ from the thin film/substrate interface, where T is the film thickness, and with each of the three dipole orientations.

4.3.2 Angular Distribution of Emission from a Dipole in a Thin Film

For a dipole in a dielectric half space, the angular distribution of its emission is anisotropic. A peak in emission intensity is observed at steeper angles, and more light is emitted into the high refractive index layer. In our thin film system there are two dielectric interfaces. The refractive index in each layer, as well as the thickness of the thin film, which affects the average distance between the dipole and each of the dielectric interfaces, is expected to impact the emission properties of the dipole. The effects of film thickness on dipole emission are explored here.

First, emission from a 100 nm thin film is analyzed. The electric field map, similar to the ones given in Figure 4.3, is shown in Figure 4.5. In this figure, the electric field intensity is averaged over three dipole orientations and three dipole heights, nine simulations in total. Figure 4.5(a) shows emission intensity into the substrate, while Figure 4.5(b) shows emission intensity into the air. In both the substrate and the air, we see rotational symmetry in the XY plane. For an isotropic dipole in a homogeneous thin film, the system is rotationally symmetric in the XY plane, so the observation of rotational symmetry in the angular distribution of emission from such a dipole is expected.

An emission peak at steep angles into the substrate is observed. This is promising for LSC performance, as this peak occurs at angles steeper than the critical angle between the substrate and air, meaning light emitted at such angles is trapped in the concentrator. Also promising, the emission intensity into the substrate is much higher than the emission intensity into the air. This behavior is necessary in thin film LSCs to avoid prohibitive escape cone losses, as none of the fluorescent light emitted directly into the air can reach the solar cells at the edge of the substrate. Another interesting observation is the similarity between the behavior of emission in a thin film and emission in a half space. Although there is an intermediate layer—the thin film—in which the dipole is placed, the angular distribution of emission from a dipole in a thin film resembles that of a dipole in a half space. Light is preferentially emitted into the substrate, which has a real refractive index greater than the air but less than the thin film, and there is a strong emission peak at steep angles.

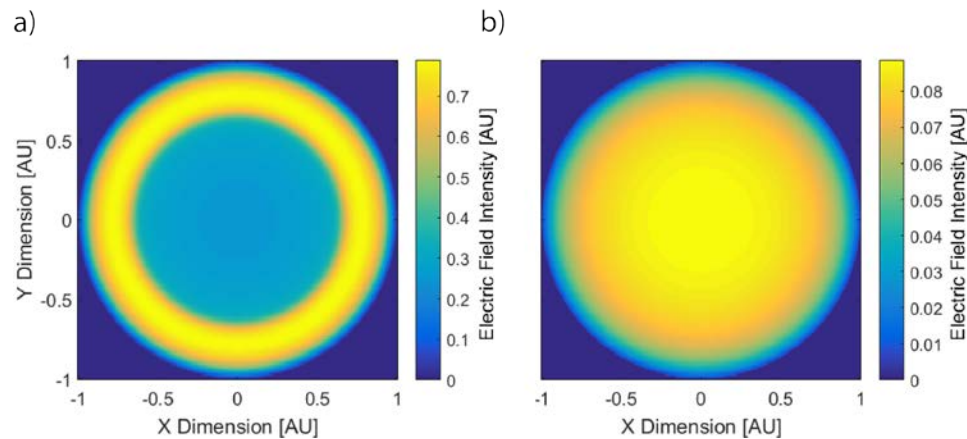


Figure 4.5 The electric field intensity map for light emitted from a dipole in a 100 nm thin film into the (a) substrate and the (b) air is shown. Emission intensity is angularly symmetric within the XY plane. A peak is observed in the substrate at steep angles, and more light is emitted into the substrate than the air.

To study the effects of film thickness on luminophore emission, the thickness of the thin film is varied from 100 nm to 1000 nm. The electric field intensity is calculated as a function of the angle between the direction of emission and the normal of the thin film/substrate interface. In this case, 0 degrees is directly into the substrate, 90 degrees points along the thin film, and 180 degrees is directly into the air. Figure 4.6 shows the angular distribution for various thin film thicknesses.

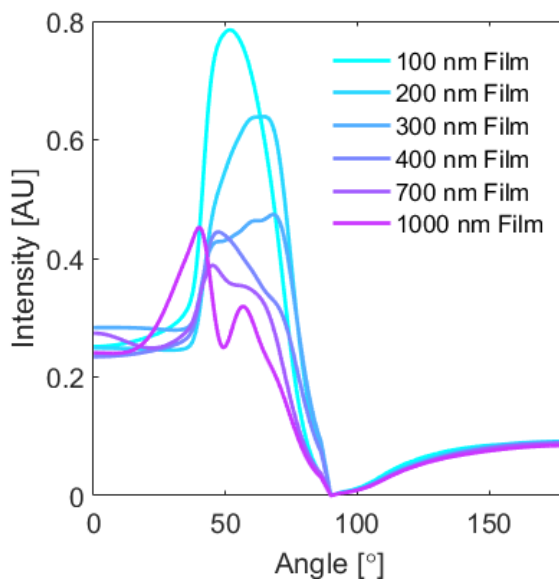


Figure 4.6 The angular distribution of emission is given for various thin film thicknesses. Emission into the substrate, normal to the thin film/substrate interface, is 0 degrees. Emission parallel to the interface is 90 degrees. Emission into the air, normal to the air/thin film interface, is 180 degrees.

As thin film thickness increases, the emission peak first shifts to steeper angles, before transitioning to smaller angles. The intensity of the emission peak steadily decreases with film thickness. Two effects are observed here. First, as film thickness increases, the emission peak shifts to steeper angles. For a non-absorbing film, we would expect to see a constant shift of the peak to steeper angles. However, the film is absorbing, as it contains

luminophores, and as film thickness increases so does reabsorption within the thin film. This reabsorption is most prominent with light emitted at steep angles. Therefore, as film thickness increases, more and more of the emission peak is lost to reabsorption, leading to the eventual shift in emission to smaller angles and the general decrease in peak intensity with film thickness. For thin film LSCs, these results indicate that films cannot be made too thick or much of the light emitted into the substrate will not be trapped by total internal reflection.

4.3.3 Reabsorption of Emission within a Thin Film

The increase of reabsorption with thin film thickness was briefly discussed in the previous section. In this section, the reabsorption of emitted light within the thin film is explored further. When light is emitted from a luminophore in an LSC, it can be reabsorbed by other luminophores reaching the edge of the device. This reabsorption is problematic, as light must be guided to the edge to be collected by the solar cells. After each reabsorption event, there is a chance for non-radiative recombination or emission into the escape cone, resulting in losses in LSC efficiency. Therefore, LSCs should be designed to minimize the number of interactions an emitted photon has with luminophores. Thin film LSCs are designed to minimize these interactions by confining the absorbing luminophores to a thin film placed on top of a glass waveguide. Once light is emitted into the glass substrate, it can propagate to the edges with minimal interactions with the thin film. However, before light is trapped in the substrate it must be emitted out of the thin film. Naturally, some of the light emitted within the thin film is reabsorbed before leaving the thin film. The effects of thin film thickness on this reabsorption is explored.

Reabsorption probability is the fraction of emitted light that does not enter the air or substrate. That is, it is the fraction of emitted light which is absorbed by the thin film. Note that for present simulations, all emitted light propagating within the thin film is absorbed before reaching the edge of the simulation region, so all light which does not enter the air or substrate has been absorbed. The reabsorption probability is calculated for varying film thickness and plotted in Figure 4.7. Increasing thin film thickness increases both the number of luminophores within the thin film, though the concentration of luminophores is constant, and the average distance between a luminophore and the air or substrate. Thus, thicker films experience greater reabsorption, with the probability of reabsorption without leaving the thin film near 45% for 1000 nm thin films. In addition to rising reabsorption with thin film thickness, oscillatory behavior is observed. The

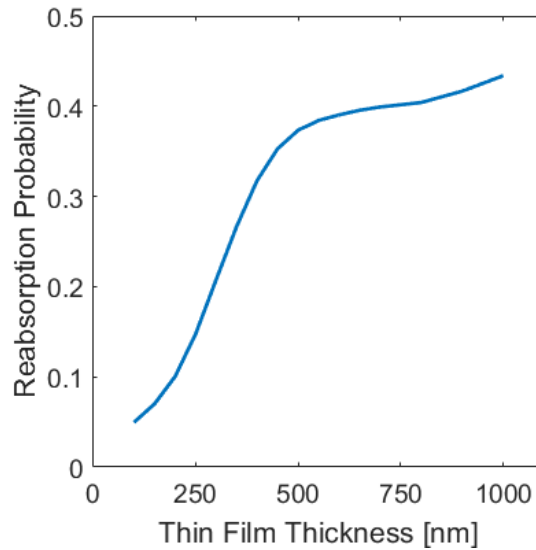


Figure 4.7 The probability of reabsorption within the thin film is shown for varying thin film thicknesses. Reabsorption is low for thinner films, but approaches 45% for thicker films, presenting a significant source of losses for an LSC.

reabsorption probability curve shows oscillations with a frequency near the wavelength of emitted light. These oscillations likely arise from the trapping of light within the thin film, as thin film reflection and transmission oscillates with thin film thickness.

4.4 Thin Film Absorption, Reflection, and Transmission

To model a thin film in the Monte Carlo algorithm, Fresnel equations and absorption data are inadequate to capture the absorption, reflection, and transmission behavior of the thin film. Light incident upon a thin film must be treated as a wave because the thickness of the thin film is on the order of the wavelength of incident light, giving rise to interference effects. Therefore, an analytical wave-optics model must be developed to calculate the absorption, reflection, and transmission of a thin film using film thickness, film and substrate refractive index data, luminophore absorption spectrum, and angle of incidence as inputs. The addition of this model into the Monte Carlo algorithm allows the algorithm to evaluate whether a photon incident upon the thin film is absorbed, reflected, or transmitted.

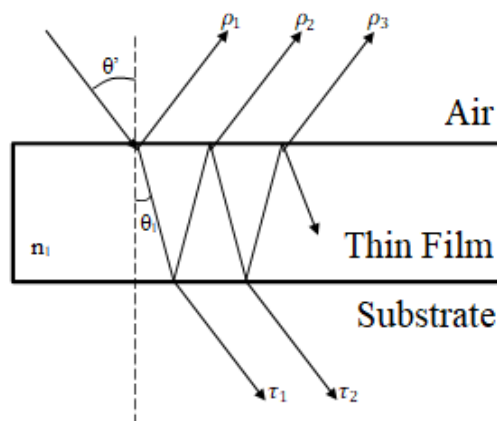


Figure 4.8 Light incident on the thin film is split into partial reflectance and transmittance waves. The sum of these waves can be used to determine the absorption, reflection, and transmission of the thin film.

The thin film is treated as an etalon, similarly to the treatment of multijunction LSCs in Section 3.2. Light incident on the thin film is divided into an infinite series of partial waves, shown in Figure 4.8. The amplitude of these partial reflectance, ρ_i , and transmittance, τ_i , waves are

$$\rho_1 = \sqrt{R_1} , \quad \rho_2 = T\sqrt{R_2}Ae^{i\delta} , \quad \rho_3 = TR_1\sqrt{R_2}A^2e^{2i\delta} , \quad \dots \quad (4.1)$$

$$\begin{aligned} \tau_1 &= \sqrt{T_1}\sqrt{T_2}A^{\frac{1}{2}} , \quad \tau_2 = \sqrt{T_1}\sqrt{T_2}\sqrt{R_1}\sqrt{R_2}A^{\frac{3}{2}}e^{i\delta} , \\ \tau_3 &= \sqrt{T_1}\sqrt{T_2}R_1R_2A^{\frac{5}{2}}e^{2i\delta} , \quad \dots \end{aligned} \quad (4.2)$$

where R_1 and R_2 are the reflectivities of the air/thin film and thin film/substrate interfaces, respectively, T_1 and T_2 are the transmissivities of the air/thin film and thin film/substrate interfaces, respectively, A is the fraction of light *not* absorbed per two passes, and δ is a phase factor given by

$$\delta = \frac{4\pi n_1 l \cos\theta_1}{\lambda} \quad (4.3)$$

where n is the index of refraction of the thin film, l is the thickness of the thin film, θ_1 is the angle of light propagation in the thin film relative to the normal and λ is the wavelength of light. Notice $T = 1 - R$.

The total amplitude of reflected light, ρ , is the sum of all partial reflected waves. With some simple algebraic manipulation ρ can be represented as the sum of a geometric series.

$$\rho = \rho_1 + \rho_2 + \rho_3 + \dots = \sqrt{R_1} - T_1\sqrt{R_2}Ae^{i\delta} - T_1\sqrt{R_1}R_2A^2e^{2i\delta} - T_1R_1R_2^{\frac{3}{2}}A^3e^{3i\delta} - \dots \quad (4.4)$$

$$= \sqrt{R_1} - T_1 \sqrt{R_2} A e^{i\delta} (1 + \sqrt{R_1} \sqrt{R_2} A e^{i\delta} + R_1 R_2 A^2 e^{2i\delta} + \dots) = \sqrt{R_1} - \frac{T_1 \sqrt{R_2} A e^{i\delta}}{1 - \sqrt{R_1} \sqrt{R_2} A e^{i\delta}}$$

Here we used a simple geometric series formula valid for any $|x| < 1$, namely

$$1 + x + x^2 + \dots = \frac{1}{1-x} \quad (4.5)$$

The intensity of light reflected, I_r is equal to the product of the total amplitude of reflected light and its complex conjugate. Shown below is the equation for I_r .

$$\begin{aligned} I_{rT} &= \rho \rho^* = \left(\sqrt{R_1} - \frac{T_1 \sqrt{R_2} A e^{i\delta}}{1 - \sqrt{R_1} \sqrt{R_2} A e^{i\delta}} \right) \left(\sqrt{R_1} - \frac{T_1 \sqrt{R_2} A e^{-i\delta}}{1 - \sqrt{R_1} \sqrt{R_2} A e^{-i\delta}} \right) \quad (4.6) \\ &= \left(\frac{\sqrt{R_1} - R_1 \sqrt{R_2} A e^{i\delta} - (1 - R_1) \sqrt{R_2} A e^{i\delta}}{1 - \sqrt{R_1} \sqrt{R_2} A e^{i\delta}} \right) \left(\frac{\sqrt{R_1} - R_1 \sqrt{R_2} A e^{-i\delta} - (1 - R_1) \sqrt{R_2} A e^{-i\delta}}{1 - \sqrt{R_1} \sqrt{R_2} A e^{-i\delta}} \right) \\ &= \left(\frac{\sqrt{R_1} - \sqrt{R_2} A e^{i\delta}}{1 - \sqrt{R_1} \sqrt{R_2} A e^{i\delta}} \right) \left(\frac{\sqrt{R_1} - \sqrt{R_2} A e^{-i\delta}}{1 - \sqrt{R_1} \sqrt{R_2} A e^{-i\delta}} \right) \\ &= \frac{R_1 + R_2 A^2 e^{i\delta} - \sqrt{R_1} \sqrt{R_2} A (e^{i\delta} + e^{-i\delta})}{1 + R_1 R_2 A^2 - \sqrt{R_1} \sqrt{R_2} A (e^{i\delta} + e^{-i\delta})} \\ &= \frac{(\sqrt{R_1} - \sqrt{R_2} A)^2 + 2\sqrt{R_1} \sqrt{R_2} A - \sqrt{R_1} \sqrt{R_2} A (e^{i\delta} + e^{-i\delta})}{(1 - \sqrt{R_1} \sqrt{R_2} A)^2 + 2\sqrt{R_1} \sqrt{R_2} A - \sqrt{R_1} \sqrt{R_2} A (e^{i\delta} + e^{-i\delta})} \\ &= \frac{(\sqrt{R_1} - \sqrt{R_2} A)^2 + 2\sqrt{R_1} \sqrt{R_2} A (1 - \cos(\delta))}{(1 - \sqrt{R_1} \sqrt{R_2} A)^2 + 2\sqrt{R_1} \sqrt{R_2} A (1 - \cos(\delta))} \\ &= \frac{(\sqrt{R_1} - \sqrt{R_2} A)^2 + 4\sqrt{R_1} \sqrt{R_2} A \sin^2\left(\frac{\delta}{2}\right)}{(1 - \sqrt{R_1} \sqrt{R_2} A)^2 + 4\sqrt{R_1} \sqrt{R_2} A \sin^2\left(\frac{\delta}{2}\right)} \end{aligned}$$

This method can be repeated for transmissivity to obtain the intensity of light transmitted, I_t . The intensity of light absorbed, I_a , is then the difference between 1 and the intensities of light reflected and transmitted. The results of those procedures are shown below.

$$I_t = \frac{(1-R_1)(1-R_2)A^2}{(1-\sqrt{R_1}\sqrt{R_2}A)^2 + 4\sqrt{R_1}\sqrt{R_2}A\sin^2\left(\frac{\delta}{2}\right)} \quad (4.7)$$

$$I_a = 1 - I_{rT} - I_{tT} \quad (4.8)$$

4.5 Thin Film LSC Monte Carlo Simulations

After studying the effects of a thin film architecture on luminophore emission and reabsorption, and calculating thin film absorption, reflection and transmission, the results from those simulations are integrated into a Monte Carlo ray-tracing model to evaluate the performance of thin film LSCs. When photons reach the thin film, equations 4.6–4.8 from Section 4.4 are used to determine whether the photons were absorbed, reflected, or transmitted. Absorbed photons can be emitted, with a certain probability of being reabsorbed without leaving the thin film, determined by the results in Section 4.3.3. Photons that are emitted without being reabsorbed have an angular distribution determined by the simulations in Section 4.3.2.

Monte Carlo simulations are performed for a 1 m x 1 m thin film LSC with a 100 nm thick film embedded with CdSe/CdS quantum dots where QY = 75%, OD = 0.033 at 450 nm. No mirrors are placed above or beneath the LSC. The results of the simulations are shown in Figure 4.9(a). The collection mechanisms of absorbed light are tracked and are shown in Figure 4.9(b). Unabsorbed losses present the largest loss mechanism in this

system, as a majority of incident light passes through the concentrator without being absorbed due to the low optical density of the thin film. Unabsorbed losses could be decreased by increasing the thickness of the thin film, increasing the concentration of luminophores in the film, or with the addition of a back mirror to reflect transmitted light back into the concentrator. Aside from transmitted light, reflection is another major loss mechanism. Reflection losses are more prominent here compared to bulk polymer LSCs because the real refractive index of the thin film is higher than that of a bulk polymer, leading to higher Fresnel reflection. Of the light that enters into the concentrator and is absorbed, almost 40% of the light is emitted and guided to the solar cell. Reabsorption and escape cone losses are relatively small, with roughly 1/3 of absorbed light being lost to these mechanisms. The collection mechanisms of absorbed light shown in Figure 4.9(b) is independent of incident photon wavelength as quantum yield and emission wavelength is

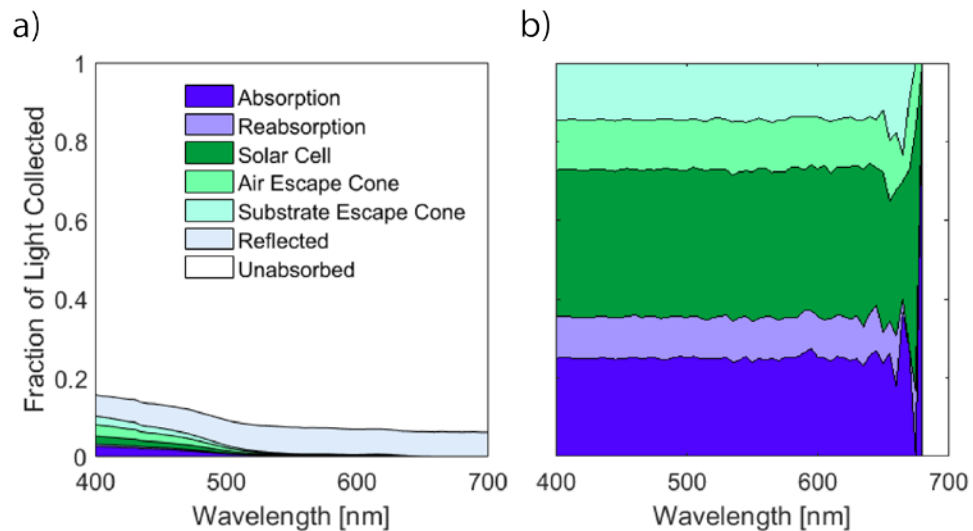


Figure 4.9 Monte Carlo simulation results for a 1 m x 1 m thin film LSC with a thin film thickness of 100 nm, CdSe/CdS QY of 75%, and OD of 0.033 at 450 nm. Simulations results were shown for (a) all incident light, and (b) absorbed light.

independent of incident wavelength. A lot of noise exists near 700 nm because few photons are absorbed at these wavelengths.

Simulations are run for thin film LSCs with varying thin film thicknesses. For these simulations, the concentration of luminophores in the thin film is held constant, meaning the optical density of the film increases with film thickness. Analogous simulations are run for a bulk polymer LSC with the same quantum yield, LSC dimensions, and optical densities. The fraction of light collected at the edge is calculated for each LSC architecture and weighted by the solar spectrum. A plot of edge collection against optical density, which correlates to film thickness for the thin film LSC, is given in Figure 4.10. Note that OD =

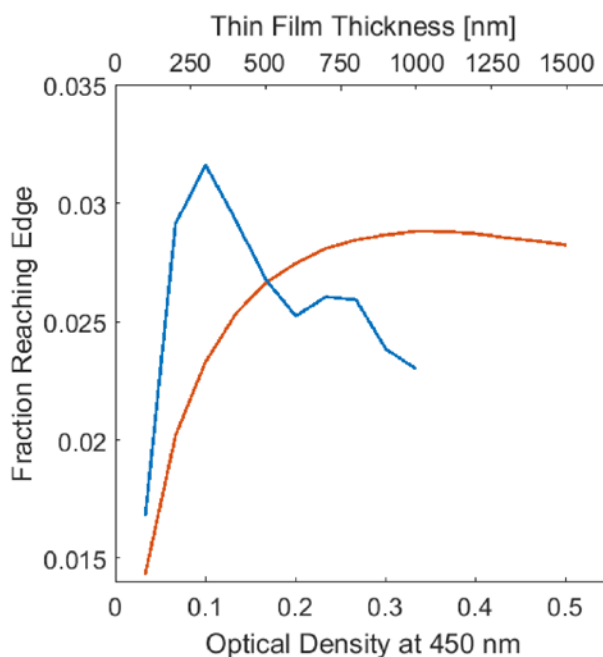


Figure 4.10 The fraction of light reaching the edge of a thin film (blue) and bulk polymer (orange) LSC, weighted by the solar spectrum, is plotted against optical density at 450 nm. The top x axis shows corresponding film thicknesses for the thin film. At small thickness/ODs, the thin film provides superior performance, though the bulk polymer LSC outperforms the thin film design at larger thicknesses/ODs.

0.033 (at 450 nm) correlates to a film thickness of 100 nm and $OD = 0.334$ correlates to a film thickness of 1000 nm. Both the thin film LSC and the bulk polymer LSC show an increase in edge collection up to an optimal film thickness/OD, and then a decrease. The optimal OD is much smaller for the thin film LSC, around 0.10, than the bulk polymer LSC, around 0.35. For the thin film LSC, low reabsorption combined with preferential emission at steep angles contributes to the low optimal OD.

For small ODs, the thin film LSC is able to outperform the bulk polymer LSC by decreasing escape cone and reabsorption losses, see Figure 4.11. However, as OD increases, reabsorption within the thin film leads to higher reabsorption losses and reduces the emission peak at steep angles, increasing escape cone losses. This leads to a decrease in thin film performance relative to the bulk polymer, causing the bulk polymer LSC to

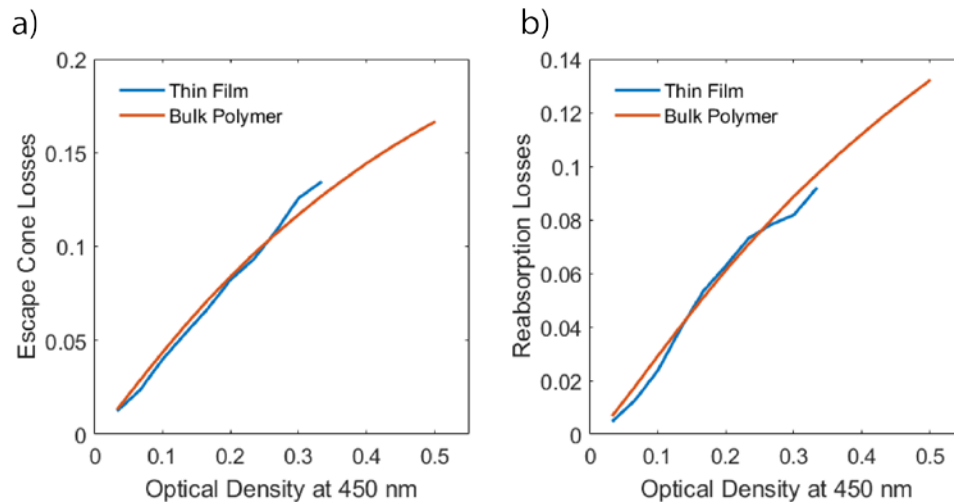


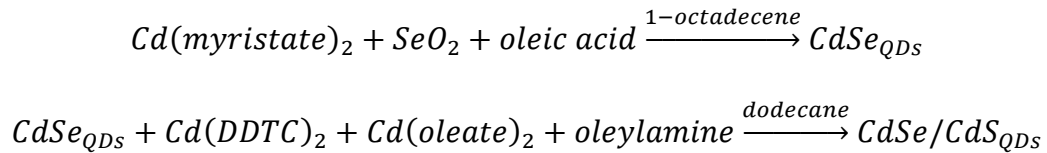
Figure 4.11 (a) Escape cone and (b) reabsorption losses are given for the thin film and bulk polymer LSCs for varying film thickness/OD. Preferential emission at steep angles leads to a reduction in escape cone losses for the thin film LSC at low OD. Emission is effectively coupled into the substrate for the thin film LSC with low OD, leading to a reduction in reabsorption losses, as light can propagate primarily through the lossless glass substrate.

overtake the thin film LSC in edge collection around $OD = 0.175$. The best performance achieved in these simulations is for the thin film LSC with a thin film thickness of 300 nm ($OD = 0.10$ nm), demonstrating the benefits offered by a thin film architecture. However, the superior efficiency of the bulk polymer at larger ODs shows the need to understand the thin film system in order to achieve these benefits.

Chapter 5. Thin Film LSC Experiments

In conjunction with simulations, thin film LSCs are fabricated and tested experimentally. CdSe/CdS core-shell quantum dots are synthesized using a colloidal method and characterized. Quantum dots are then dispersed in a polymer solution and deposited onto a glass substrate, forming an LSC. The optical properties of the LSC are characterized and experiments are performed to study the guiding properties of the concentrator.

5.1 CdSe/CdS Quantum Dot Synthesis



A previously-reported non-injection method is used to synthesize colloidal CdSe/CdS core-shell quantum dots [71], [76]. Equimolar amounts of cadmium myristate and selenium dioxide are dissolved in 1-octadecene at room temperature. The resulting solution is degassed to remove any water and air dissolved in the solvent. The solution is then placed under nitrogen and heated to 240 °C. During heating, the milky solution turns clear and colorless before gradually transitioning from to yellow, orange, bright red, and finally a dark red. Oleic acid ligands are injected into the heated solution dropwise in a 3:1 molar ratio to the cadmium and selenium precursors. The solution is then cooled to room temperature. Quantum dots are crashed out of solution using acetone and re-dispersed in toluene to remove unreacted precursors and excess ligands. The absorbance spectrum of these CdSe quantum dots are shown in Figure 5.1. The first excitonic peak is seen at 584

nm, while other excitonic features are observed at 405 nm, 474 nm, and 547 nm. UV-VIS correlations reported in Reference [77] are used to calculate the average size of the quantum dots, which is 3.7 nm.

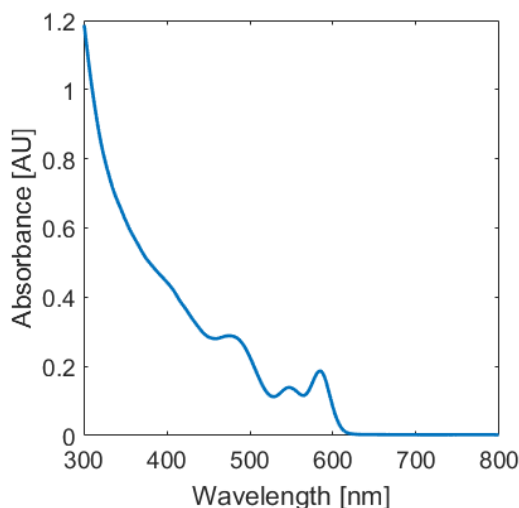


Figure 5.1 The absorbance spectrum of CdSe quantum dots is given. The first excitonic feature is seen at 584 nm.

CdS shells are added to the CdSe quantum dots in solution by creating a cadmium and sulfur precursor solution and performing a series of injections to a solution of CdSe cores. Dodecane and oleylamine are mixed and degassed to remove dissolved gasses. CdSe quantum dots dissolved in toluene are added to the solution air free, and the solution is degassed again. A cadmium and sulfur precursor solution is made by mixing dodecane, oleylamine, cadmium diethyldithiocarbamate, and cadmium oleate and then degassing. The quantum dot solution is heated to 80 °C and enough precursor solution is injected to form one monolayer of CdS shell. The solution is then heated to 160 °C, held for 20 minutes, and cooled to 80 °C. These injections are repeated until the desired number of

monolayers was achieved. After injections, nitrogen gas is bubbled through the CdSe/CdS quantum dot solution. Cadmium chloride is injected to passivate the surface of the quantum dots. The quantum dots are crashed out of solution using acetone and re-dispersed in hexane or octane.

5.2 CdSe/CdS Quantum Dot Characterization

The optical properties of synthesized quantum dots are characterized. TEM images are taken to determine the size distribution of quantum dots. Figure 5.2 shows an image of the quantum dots and the size distribution calculated from TEM images. The quantum dots are slightly ellipsoidal with an average diameter of 9.3 ± 1.2 nm, corresponding to an 8 monolayer CdS shell.

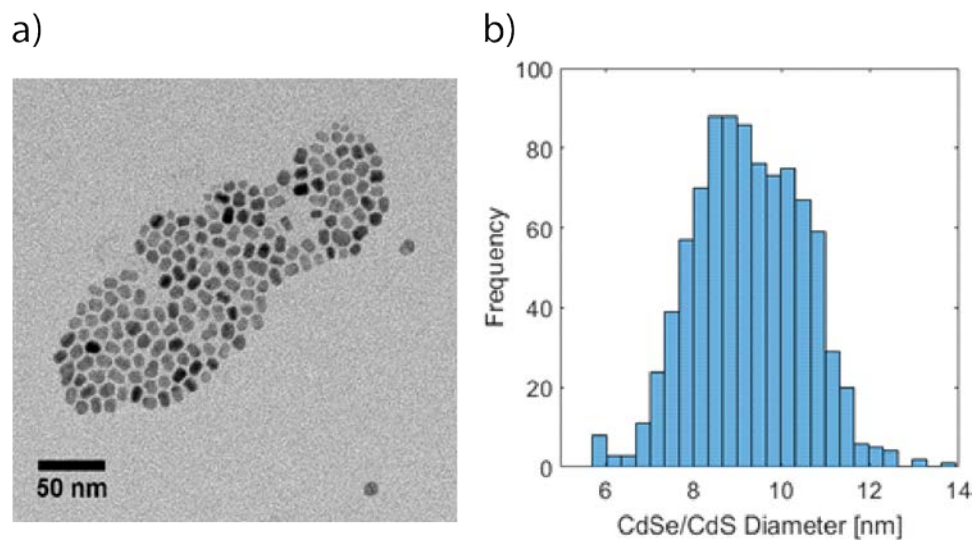


Figure 5.2 (a) A TEM image of CdSe/CdS quantum dots is given. The quantum dots are slightly ellipsoidal. (b) The size distribution of the quantum dots, determined from TEM images, is shown. The average quantum dot size was 9.3 ± 1.2 nm.

The absorbance and emission spectra of the quantum dots in hexane are measured using UV-VIS and fluorescence spectroscopy, respectively. These spectra are given in Figure 5.3. The first excitonic feature of the absorption spectrum occurs at 625 nm, red-shifted from the CdSe cores, which exhibit their first excitonic peak at 584 nm. The excitonic absorbance features of the CdSe cores are suppressed by CdS shell, reducing overlap between the absorption and emission spectra, which is important for LSC applications. The emission spectrum of the quantum dots has an emission peak at 644 nm with a FWHM of 36 nm.

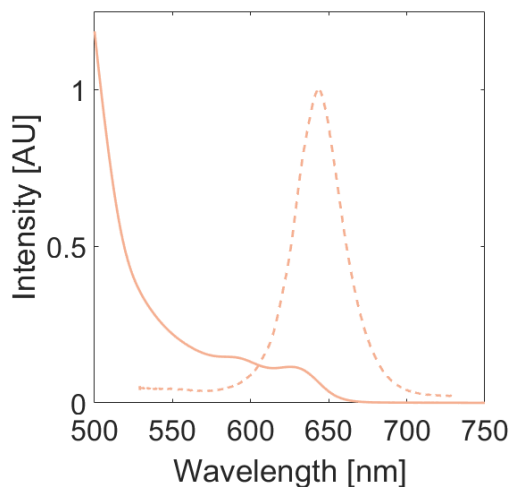


Figure 5.3 The absorbance (solid) and emission (dotted) spectra of CdSe/CdS is shown. A weak excitonic peak is observed at 625 nm, while the emission peak occurs at 644 nm.

The fluorescent lifetime of the quantum dots is measured to determine the average lifetime of an excited electron. Nonradiative recombination mechanisms are generally faster than radiative recombination, so longer lifetimes correlate to more emission. The fluorescent lifetime of the quantum dots is measured as 37 ± 1 ns. Quantum yield

measurements are taken to directly measure emission efficiency. The CdSe/CdS quantum dots had a quantum yield of 67%.

5.3 Thin Film Fabrication and Characterization

Once CdSe/CdS core-shell quantum dots are fabricated and characterized, they are dispersed into a polymer solution and deposited onto a glass substrate to form a thin film LSC. Poly(cyclohexylethylene) (PCHE) is chosen as it is an optically clear polymer with minimal scattering, and it is soluble in the nonpolar solvents used to synthesize the quantum dots. PCHE is dissolved in octane and filtered. The PCHE polymer solution is added to quantum dots in octane. The resulting quantum dot-PCHE solution is filtered to remove aggregates and spin cast onto a 2.54 cm x 2.54 cm x 0.1 cm glass substrate. The fluorescent lifetime of quantum dots in the thin film is 20.2 ± 0.3 ns, a significant decrease from

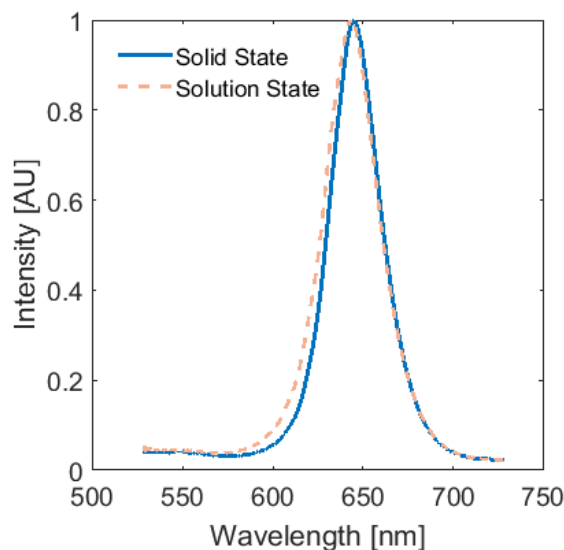


Figure 5.4 The emission spectrum of quantum dots in (pink, dotted) solution and (blue, solid) PCHE are plotted. The solid state emission spectrum contains an emission peak at 645 nm with FWHM 33 nm. Peak wavelength and width are similar to corresponding solution state measurements.

solution state measurements. The emission spectrum, however, is preserved upon dispersion into PCHE. The spectrum, shown in Figure 5.4, has a peak at 645 nm with a FWHM of 33 nm.

5.4 Effects of Thin Film Thickness on LSC Optical Properties

In this section, the optical properties of two LSCs with similar absorption but varying film thickness are compared. Thin film LSCs are prepared using the fabrication method described in Section 5.3. The concentrations of quantum dots and PCHE in the quantum dot-PCHE solution are varied to tune the thickness and optical density of the films. The volume percent of quantum dots in the thinner film is $13.0 \pm 0.1 \%$ and the volume percent of quantum dots in the thicker film is $8.5 \pm 0.1 \%$, determined by ellipsometry, discussed later in this section. Reflection and transmission measurements are taken to calculate the extinction of the LSC. For these measurements, light is incident at an

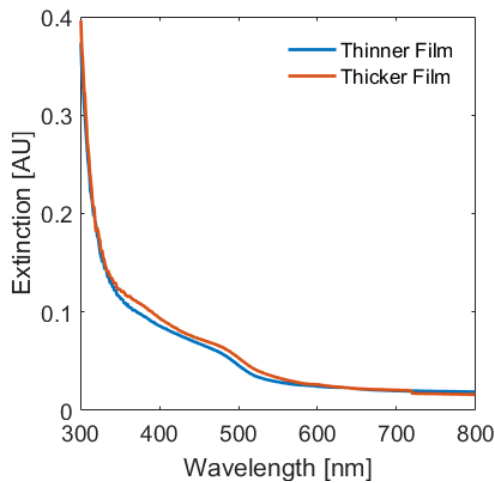


Figure 5.5 The extinction spectra of the thinner and thicker film is calculated from reflection and transmission measurements taken with light incident 6 degrees from the surface normal. Similar extinction is shown for both films.

angle of 6 degrees from the LSC surface normal. The extinction spectra of the two films, denoted “thinner” and “thicker,” are shown in Figure 5.5. The thicker film absorbs slightly more light, but the difference in absorption is small.

Spectroscopic ellipsometry is used to measure the film thickness and refractive index of each film. For these measurements, glass substrates cannot be used as reflection from the back surface of the glass interferes with thin film reflection. Therefore, films are deposited onto 2.54 cm x 2.54 cm silicon wafers using the same quantum dot-PCHE solutions and processing conditions used during thin film LSC fabrication. Spectroscopic ellipsometry measurements are taken for wavelengths between 400 nm and 790 nm. Data is fit to a Maxwell-Garnett model which is used to determine the thickness and volume fraction of quantum dots in each film. The volume fraction, refractive index of PCHE, and intrinsic refractive index of the quantum dots is then used to calculate the refractive index of the films. The thickness of the thinner film is 82.6 ± 0.1 nm; the thickness of the thicker film is 322.8 ± 0.7 nm. The refractive index of each film is shown in Figure 5.6. The real

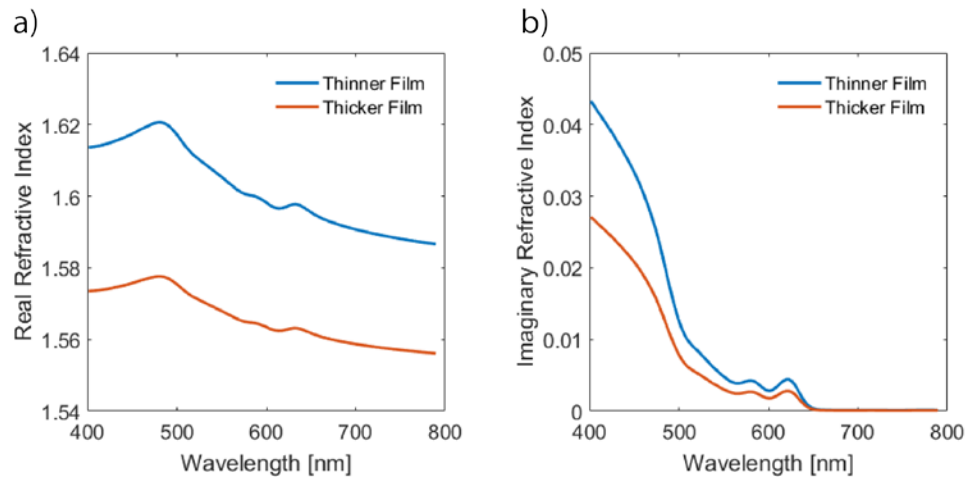


Figure 5.6 The (a) real and (b) imaginary components of refractive index are given for each film.

and imaginary component of the refractive index is larger for the thinner film than the thicker. Since the thinner film has similar extinction as the thicker, but is 3–4 times thinner, the concentration of quantum dots is larger in the thinner film. This increases the refractive index of the thin film, as the refractive index of the quantum dots is larger than PCHE.

Thin film reflection and transmission are found to vary with thin film thickness in Chapter 4. Interference effects within the thin film give rise to destructive or constructive interference which can increase or decrease reflection. These interference effects depend on the wavelength and angle of incident light, and the thickness of the thin film. Angle-dependent reflection measurements are performed to determine how the reflection spectrum changes with thin film thickness. Figure 5.7 shows the dependence of reflection on incident angle and wavelength for the (a) thinner and (b) thicker film. Oscillatory behavior with respect to incident wavelength is observed for each film. However, the

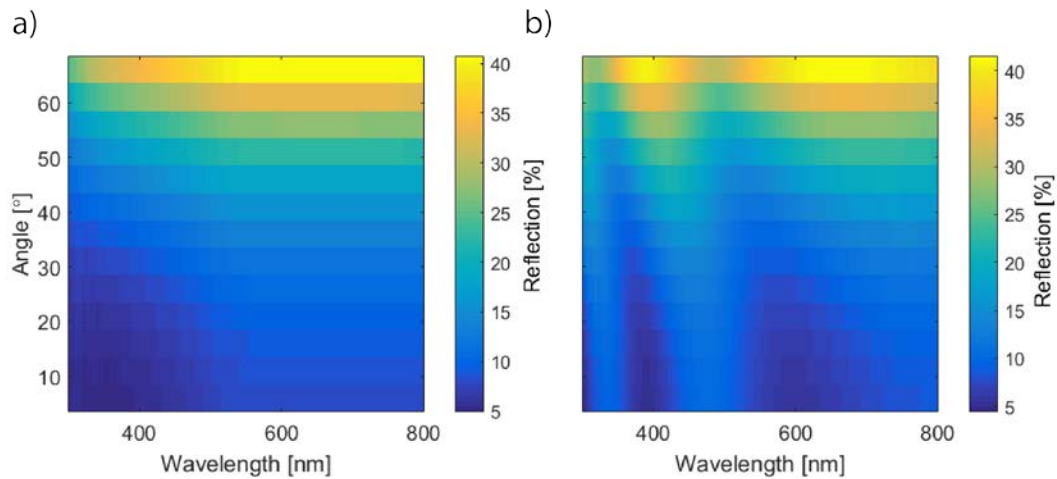


Figure 5.7 Reflection by the (a) thinner and (b) thicker film is plotted with respect to wavelength and incident angle. Oscillations are observed in both spectra.

frequencies of these oscillations vary between the thinner film, which has low frequency

oscillations, and the thicker film, which has higher frequency oscillations. For both films, reflection is larger at steeper angles, and the reflection peak blue-shifts with incident angle.

5.5 Light Guiding in Thin Film LSCs

Simulations presented in Chapter 4 suggest LSC performance varies with thin film thickness. Thinner films were shown to experience fewer reabsorption and escape cone losses. To test the light guiding properties of thin film LSCs with different film thickness, the attenuation of edge collection with illumination distance from the edge is measured for the two LSCs described in Section 5.4. In these experiments, light from a 405 nm laser is swept back and forth along the lateral dimension of the concentrator. The edge of the LSC is connected to an integrating sphere which collects light reaching the edge.

The intensity of edge collection can be plotted against the distance of the beam spot from the edge. This plot is shown in Figure 5.8(a). We see an exponential decrease in edge collection with illumination position. A more gradual decay indicates good guiding efficiency, while a steep decay indicates light is not guided far before leaving the concentrator. Here, we see similar attenuation for both the thinner and thicker film. Thus, the light guiding properties of the thin films appear to be similar. It should be noted that edge collection intensity does not decay to zero, but some finite value between 25 and 30% of collection intensity near the edge. This shows that some light is emitted outside of the absorption band of the luminophores and trapped in the LSC. Such light can propagate large distances without being disturbed by reabsorption or scattering.

In addition to edge collection intensity, the collection spectrum is measured. Each spectrum is fitted to a Gaussian, and the center wavelength of the Gaussian peaks is plotted

against position from the edge in Figure 5.8(b). Again, we see similar results for each of the thin films. A slight red-shift in center wavelength is observed. Reabsorption naturally increases as the average path length of photons reaching the edge increases. As light with shorter wavelengths are more readily reabsorbed by the luminophores, this leads to the observed red-shift of center wavelength. It should be noted that this shift is small, less than 1 nm, which indicates little reabsorption within the thin films.

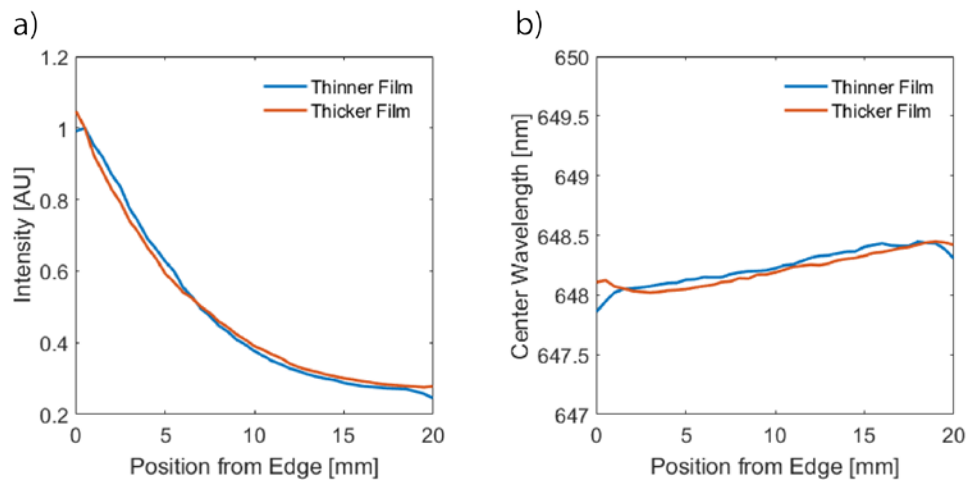


Figure 5.8 (a) Attenuation measurements are given for the thinner and thicker film. Each film shows an exponential decay in edge collection intensity with illumination position. The decay of each film is similar, pointing toward similar light guiding properties. (b) The center wavelength of the edge collection spectrum is shown. Both films show a slight red-shift with position as more light at shorter wavelengths are reabsorbed.

Chapter 6. Conclusions and Future Work

The potential for light management strategies to provide efficiency improvements in LSCs has been explored in this thesis. This work has focused on three light management strategies: wavelength-selective mirrors, multijunction LSCs, and the thin film architecture. Design considerations were examined for aperiodic wavelength-selective top mirrors to increase light trapping. Spectrum splitting was achieved using a multijunction configuration to increase absorption and decrease thermalization. Finally, thin film effects were demonstrated to increase light trapping and light guiding. In this chapter, suggestions are discussed for future work in multijunction and thin film LSC architectures. Potential intermediate reflector designs are presented and next steps for simulations and experimental work continuing thin film LSC studies are discussed.

6.1 Intermediate Reflectors for Multijunction LSCs

Reflecting layers can be used in LSCs to increase light absorption and decrease escape cone losses. A mirror can be placed beneath the LSC to reflect unabsorbed light and light emitted into the escape cone back into the concentrator. A wavelength-selective mirror can be placed above the LSC to reflect emitted light while transmitting light within the absorption band. Multijunction LSCs present a third opportunity for efficiency-enhancing mirror: an intermediate reflector placed in between LSC layers. Intermediate reflectors have been used extensively in multijunction solar cells to aid in current matching by reflecting some of the incident light back into the top solar cell, increasing top layer absorption. These intermediate reflectors can provide wavelength-independent reflection, as with thin films which exhibit Fresnel reflection [78]–[82], or wavelength-selective

reflection, as with 1D and 3D photonic crystals [40], [46]–[49], [83], [84]. Two classes of intermediate reflectors are discussed here.

The first intermediate reflector is a 3D photonic crystal reflector designed to increase light absorption and provide trapping of bottom layer emission. 3D photonic crystals are periodic arrangements of nanoscale dielectric building blocks which provide wavelength-selective reflection via interference effects similar to the top mirrors used in Chapter 2. However, these 3D arrangements offer additional optical properties such of forward scattering of transmitted light and the absence of the blue-shifting effect in their reflection band with angle of incidence. These additional properties provide light absorption benefits by increasing bottom layer absorption through scattering and providing consistent reflection at all angles of incidence.

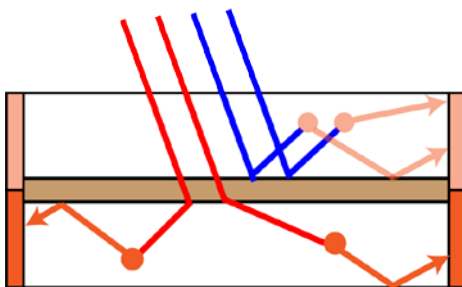


Figure 6.1 An intermediate reflector consisting of a 3D photonic crystal (brown) can be designed to increase light absorption in both layer, decrease thermalization, and increase bottom layer trapping.

Intermediate reflectors consisting of 3D photonic crystals can be designed to reflect high energy light back into the top layer, reducing thermalization and increasing top layer absorption, forward scatter light transmitted into the bottom layer to increase absorption there, and reflect low energy light emitted from bottom layer luminophores. These effects,

summarized in Figure 6.1, combine to increase light absorption and trapping. Increasing light absorption not only decreases unabsorbed losses in the concentrators, but shifts the optimum optical density of the layers to lower values, decreasing reabsorption losses as well. Increased trapping in the bottom layer decreases escape cone losses from bottom layer emission.

The second intermediate reflector proposed is a beam-guiding metasurface. Metasurfaces are nanostructure materials consisting of a periodic array of nanofeatures which give rise to unique optical properties [85]. By choosing the appropriate geometry and material properties the phase, amplitude, and polarization of light can be controlled [86], [87]. For LSC applications, avoiding parasitic light absorption by the intermediate reflector is critical, so dielectric metasurfaces are required. Such reflectors can be used to tune the angle of transmitted and reflected light [88]–[91].

A beam-guiding metasurface can be designed to steer transmitted light towards the edge of the concentrator, serving to decrease reabsorption by decreasing the path length of trapped light while increasing absorption by increasing the path length of incident light. These two effects are shown in Figure 6.2. Light reflected off the metasurface featuring a phase gradient is guided to the edge by imparting a phase shift which increases the angle of reflected light. The angle of reflected light is determined by generalized Snell’s law [70], shown in Equation 6.1. References [92] and [93] show two examples of nanodisk and nanoblock arrays designed to steer transmission through the metasurface to desired angles.

$$\sin(\theta_r) - \sin(\theta_i) = n_i^{-1} \lambda \nabla \Phi / 2\pi \quad (6.1)$$

where θ_r and θ_i are the reflected and incident angles, n_i is the index of refraction of the surrounding medium, λ is the wavelength of light and $\nabla\Phi$ is the phase gradient.

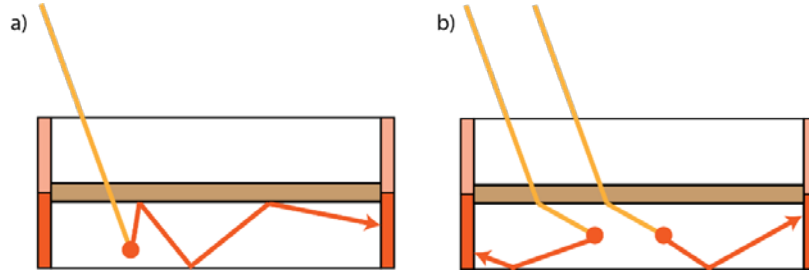


Figure 6.2 (a) Metasurfaces impart a phase shift upon reflection, providing anomalous reflection and guiding light to the edge. (b) Light transmitted through the metasurface is refracted at large angles, increasing light absorption.

6.2 Thin Film LSCs

Present work has demonstrated the effects of thin film geometry on LSC performance. Simulations were performed for LSCs with varying film thicknesses. In these simulations, the concentration of quantum dots in the polymer film were held constant, meaning as thin film thickness increased, so did optical density. This creates a convolution of effects when evaluating how film thickness and optical density affect LSC performance. This is perhaps most evident in Figure 4.6, where the angular distribution of emitted light is shown for varying thin film thicknesses. In this plot, we observed the emission peak begin to shift to large angles as film thickness increased, then shift to lower angles as light at large angles was reabsorbed. From these simulations, it is difficult to discern whether how much of this problematic reabsorption is due to film thickness versus an increase in thin film optical density.

In order to deconvolute thin film thickness from optical density, simulations could be run with varying quantum dot concentration, allowing thin film thickness to vary while holding optical density constant or vice versa. Such simulations are made difficult, however, by changes in thin film refractive index with quantum dot concentration. Several thin films with different concentrations can be fabricated and measured using spectroscopic ellipsometry to create a dataset with refractive index data for several concentrations. These data can be imported into the FDTD model and used to simulate with varying thickness and constant optical density, or varying optical density and constant thickness. Results from these simulations can be analyzed to determine thin film reabsorption and the angular distribution of emission, and implemented into Monte Carlo simulations to study LSC performance.

Experimentally, two thin films have been fabricated with different film thicknesses and similar optical density. A larger set of film thicknesses could be fabricated to study a wider range of thicknesses. Additionally, thin films can be fabricated with constant film thickness but varying optical density to study the effects of quantum dots concentration on light guiding and emission. A set of bulk polymer LSCs could be made to directly compare the performance of thin film and bulk polymer LSCs, demonstrating the differences shown in simulations.

6.3 Conclusion

Luminescent solar concentrators provide an opportunity for efficient building-integrated photovoltaics due to their versatility in design and ability to effectively collect and concentrate direct and diffuse sunlight. Light management systems are a crucial

component of LSCs which can serve to increase light absorption and decrease several prominent loss mechanisms like reabsorption and escape cone losses. This work has shown how three of these light management strategies can be used to boost LSC performance significantly. Design considerations for aperiodic top mirrors were explored to maximize light trapping while maintaining high light absorption. Two LSC layers were stacked to form a multijunction LSC. Thermalization losses were reduced while broadening the absorption band of the LSC system. Finally, wave optics effects were studied for a thin film LSC geometry. The emission and guiding properties of this architecture were examined and the potential of these concentrator to provide superior performance over traditional bulk polymer concentrators was demonstrated. Ultimately, in this work we see the potential for light management strategies to produce high efficiency luminescent solar concentrators and the breadth of such strategies available to achieve this goal.

Bibliography

- [1] “Electric Power Monthly,” *U.S. Energy Information Administration*, 24-Jul-2018. [Online]. Available: https://www.eia.gov/electricity/monthly/epm_table_grapher.php?t=epmt_1_17_b. [Accessed: 16-Aug-2018].
- [2] “Annual Energy Outlook 2017 with projections to 2050,” *U.S. Energy Information Administration*, 05-Jan-2017. [Online]. Available: [https://www.eia.gov/outlooks/aeo/pdf/0383\(2017\).pdf](https://www.eia.gov/outlooks/aeo/pdf/0383(2017).pdf). [Accessed: 16-Aug-2018].
- [3] S. A. Mann, R. R. Grote, R. M. Osgood, A. Alù, and E. C. Garnett, “Opportunities and Limitations for Nanophotonic Structures To Exceed the Shockley–Queisser Limit,” *ACS Nano*, vol. 10, no. 9, pp. 8620–8631, Sep. 2016.
- [4] M. K. Assadi *et al.*, “Enhancing the efficiency of luminescent solar concentrators (LSCs),” *Appl. Phys. A*, vol. 122, no. 9, p. 821, Sep. 2016.
- [5] S. P. Philipps, A. W. Bett, K. Horowitz, and S. Kurtz, “Current Status of Concentrator Photovoltaic (CPV) Technology,” National Renewable Energy Lab. (NREL), Golden, CO (United States), NREL/TP-5J00-65130, Dec. 2015.
- [6] K. Shanks, S. Senthilarasu, and T. K. Mallick, “Optics for concentrating photovoltaics: Trends, limits and opportunities for materials and design,” *Renew. Sustain. Energy Rev.*, vol. 60, pp. 394–407, Jul. 2016.
- [7] J. H. Jo, R. Waszak, and M. Shawgo, “Feasibility of Concentrated Photovoltaic Systems (CPV) in Various United States Geographic Locations,” *Energy Technol. Policy*, vol. 1, no. 1, pp. 84–90, Jan. 2014.
- [8] A. Luque and V. M. Andreev, Eds., *Concentrator photovoltaics*. Berlin: Springer, 2007.
- [9] A. Antonini, M. Stefancich, J. Coventry, and A. Parretta, “Modelling of Compound Parabolic Concentrators for Photovoltaic Applications,” *Int. J. Opt. Appl.*, vol. 3, no. 4, pp. 40–52, 2013.
- [10] “Thirty Years of Luminescent Solar Concentrator Research: Solar Energy for the Built Environment - Debije - 2012 - Advanced Energy Materials - Wiley Online Library.” [Online]. Available: <https://onlinelibrary.wiley.com/doi/abs/10.1002/aenm.201100554>. [Accessed: 16-Aug-2018].
- [11] B. C. Rowan, L. R. Wilson, and B. S. Richards, “Advanced Material Concepts for Luminescent Solar Concentrators,” *IEEE J. Sel. Top. Quantum Electron.*, vol. 14, no. 5, pp. 1312–1322, Sep. 2008.
- [12] P. Pérez-Higueras and E. F. Fernández, *High Concentrator Photovoltaics: Fundamentals, Engineering and Power Plants*. Springer, 2015.
- [13] J. Foresi, A. Babej, R. Han, T. Liao, C. Wang, and D. King, “Suncore’s CPV power plant deployment in western China,” in *2014 IEEE 40th Photovoltaic Specialist Conference (PVSC)*, 2014, pp. 3282–3286.
- [14] N. Tien, S. Shin, N. X. Tien, and S. Shin, “A Novel Concentrator Photovoltaic (CPV) System with the Improvement of Irradiance Uniformity and the Capturing of Diffuse Solar Radiation,” *Appl. Sci.*, vol. 6, no. 9, p. 251, Sep. 2016.

- [15] M. G. Debije *et al.*, “Effect on the output of a luminescent solar concentrator on application of organic wavelength-selective mirrors,” *Appl. Opt.*, vol. 49, no. 4, pp. 745–751, Feb. 2010.
- [16] M. A. Dunlap, G. Cook, B. Marion, C. Riordan, and D. Renne, “Shining On: A primer on solar radiation data,” National Renewable Energy Lab., Golden, CO (United States), NREL/TP-463-4856, May 1992.
- [17] R. Connell and V. E. Ferry, “Integrating Photonics with Luminescent Solar Concentrators: Optical Transport in the Presence of Photonic Mirrors,” *J. Phys. Chem. C*, vol. 120, no. 37, pp. 20991–20997, Sep. 2016.
- [18] L. Xu, Y. Yao, N. D. Bronstein, L. Li, A. P. Alivisatos, and R. G. Nuzzo, “Enhanced Photon Collection in Luminescent Solar Concentrators with Distributed Bragg Reflectors,” *ACS Photonics*, vol. 3, no. 2, pp. 278–285, Feb. 2016.
- [19] M. Peters *et al.*, “Spectrally-Selective Photonic Structures for PV Applications,” *Energies*, vol. 3, no. 2, pp. 171–193, Jan. 2010.
- [20] J. S. Batchelder, A. H. Zewai, and T. Cole, “Luminescent solar concentrators. 1: Theory of operation and techniques for performance evaluation,” *Appl. Opt.*, vol. 18, no. 18, pp. 3090–3110, Sep. 1979.
- [21] P. P. C. Verbunt *et al.*, “Increased efficiency of luminescent solar concentrators after application of organic wavelength selective mirrors,” *Opt. Express*, vol. 20, no. 105, pp. A655–A668, Sep. 2012.
- [22] C. Tummeltshammer, A. Taylor, A. J. Kenyon, and I. Papakonstantinou, “Losses in luminescent solar concentrators unveiled,” *Sol. Energy Mater. Sol. Cells*, vol. 144, pp. 40–47, Jan. 2016.
- [23] A. Jiménez-Solano *et al.*, “Design and realization of transparent solar modules based on luminescent solar concentrators integrating nanostructured photonic crystals,” *Prog. Photovolt. Res. Appl.*, vol. 23, no. 12, pp. 1785–1792, Dec. 2015.
- [24] I. Coropceanu and M. G. Bawendi, “Core/Shell Quantum Dot Based Luminescent Solar Concentrators with Reduced Reabsorption and Enhanced Efficiency,” *Nano Lett.*, vol. 14, no. 7, pp. 4097–4101, Jul. 2014.
- [25] A. D. Vos, “Detailed balance limit of the efficiency of tandem solar cells,” *J. Phys. Appl. Phys.*, vol. 13, no. 5, p. 839, 1980.
- [26] S. Takeoka, M. Fujii, and S. Hayashi, “Size-dependent photoluminescence from surface-oxidized Si nanocrystals in a weak confinement regime,” *Phys. Rev. B*, vol. 62, no. 24, pp. 16820–16825, Dec. 2000.
- [27] T. van Buuren, L. N. Dinh, L. L. Chase, W. J. Siekhaus, and L. J. Terminello, “Changes in the Electronic Properties of Si Nanocrystals as a Function of Particle Size,” *Phys. Rev. Lett.*, vol. 80, no. 17, pp. 3803–3806, Apr. 1998.
- [28] S. Ögüt, J. R. Chelikowsky, and S. G. Louie, “Quantum Confinement and Optical Gaps in Si Nanocrystals,” *Phys. Rev. Lett.*, vol. 79, no. 9, pp. 1770–1773, Sep. 1997.
- [29] K. Wu, H. Li, and V. I. Klimov, “Tandem luminescent solar concentrators based on engineered quantum dots,” *Nat. Photonics*, vol. 12, no. 2, pp. 105–110, Feb. 2018.
- [30] K. Rurack and M. Spieles, “Fluorescence Quantum Yields of a Series of Red and Near-Infrared Dyes Emitting at 600–1000 nm,” *Anal. Chem.*, vol. 83, no. 4, pp. 1232–1242, Feb. 2011.

- [31] Y. Zhou *et al.*, “Near Infrared, Highly Efficient Luminescent Solar Concentrators,” *Adv. Energy Mater.*, vol. 6, no. 11, p. 1501913, Jun. 2016.
- [32] G. V. Shcherbatyuk, R. H. Inman, C. Wang, R. Winston, and S. Ghosh, “Viability of using near infrared PbS quantum dots as active materials in luminescent solar concentrators,” *Appl. Phys. Lett.*, vol. 96, no. 19, p. 191901, May 2010.
- [33] L. Tan *et al.*, “Ultrasmall PbS quantum dots: a facile and greener synthetic route and their high performance in luminescent solar concentrators,” *J. Mater. Chem. A*, vol. 5, no. 21, pp. 10250–10260, May 2017.
- [34] E. Lifshitz *et al.*, “Air-Stable PbSe/PbS and PbSe/PbSexS1-x Core-Shell Nanocrystal Quantum Dots and Their Applications,” *J. Phys. Chem. B*, vol. 110, no. 50, pp. 25356–25365, Dec. 2006.
- [35] M. Brumer *et al.*, “PbSe/PbS and PbSe/PbSexS1-x Core/Shell Nanocrystals,” *Adv. Funct. Mater.*, vol. 15, no. 7, pp. 1111–1116, Jul. 2005.
- [36] D. Yanover *et al.*, “Small-Sized PbSe/PbS Core/Shell Colloidal Quantum Dots,” *Chem. Mater.*, vol. 24, no. 22, pp. 4417–4423, Nov. 2012.
- [37] F. Meinardi *et al.*, “Large-area luminescent solar concentrators based on ‘Stokes-shift-engineered’ nanocrystals in a mass-polymerized PMMA matrix,” *Nat. Photonics*, vol. 8, no. 5, pp. 392–399, May 2014.
- [38] U. Rau, F. Einsele, and G. C. Glaeser, “Efficiency limits of photovoltaic fluorescent collectors,” *Appl. Phys. Lett.*, vol. 87, no. 17, p. 171101, Oct. 2005.
- [39] D. K. G. de Boer *et al.*, “Progress in phosphors and filters for luminescent solar concentrators,” *Opt. Express*, vol. 20, no. 103, pp. A395–A405, May 2012.
- [40] A. Bielawny, C. Rockstuhl, F. Lederer, and R. B. Wehrspohn, “Intermediate reflectors for enhanced top cell performance in photovoltaic thin-film tandem cells,” *Opt. Express*, vol. 17, no. 10, pp. 8439–8446, May 2009.
- [41] E. Lorenzo *et al.*, “Porous silicon-based rugate filters,” *Appl. Opt.*, vol. 44, no. 26, pp. 5415–5421, Sep. 2005.
- [42] S. Fahr, C. Ulbrich, T. Kirchartz, U. Rau, C. Rockstuhl, and F. Lederer, “Rugate filter for light-trapping in solar cells,” *Opt. Express*, vol. 16, no. 13, pp. 9332–9343, Jun. 2008.
- [43] B. G. Bovard, “Rugate filter theory: an overview,” *Appl. Opt.*, vol. 32, no. 28, pp. 5427–5442, Oct. 1993.
- [44] A. Bielawny *et al.*, “3D photonic crystal intermediate reflector for micromorph thin-film tandem solar cell,” *Phys. Status Solidi A*, vol. 205, no. 12, pp. 2796–2810, Dec. 2008.
- [45] J. F. Galisteo-López, M. Ibisate, R. Sapienza, L. S. Froufe-Pérez, Á. Blanco, and C. López, “Self-Assembled Photonic Structures,” *Adv. Mater.*, vol. 23, no. 1, pp. 30–69, Jan. 2011.
- [46] P. G. O’Brien, A. Chutinan, K. Leong, N. P. Kherani, G. A. Ozin, and S. Zukotynski, “Photonic crystal intermediate reflectors for micromorph solar cells: a comparative study,” *Opt. Express*, vol. 18, no. 5, pp. 4478–4490, Mar. 2010.
- [47] M. Scharer, X. Wu, A. Yamilov, H. Cao, and R. P. H. Chang, “Fabrication of inverted opal ZnO photonic crystals by atomic layer deposition,” *Appl. Phys. Lett.*, vol. 86, no. 15, p. 151113, Apr. 2005.

- [48] S. Knabe, N. Soleimani, T. Markvart, and G. H. Bauer, “Efficient light trapping in a fluorescence solar collector by 3D photonic crystal - Knabe - 2010 - physica status solidi (RRL) – Rapid Research Letters - Wiley Online Library,” *Phys. Status Solidi RRL-Rapid Res. Lett.*, vol. 4, no. 5–6, pp. 118–120, 2010.
- [49] M. Romanelli *et al.*, “Angle-resolved reflectivity and self-activated luminescence of 3D photonic crystals,” *J. Korean Phys. Soc.*, vol. 52, p. 1589, 2008.
- [50] A. Polman and H. A. Atwater, “Photonic design principles for ultrahigh-efficiency photovoltaics,” *Nat. Mater.*, vol. 11, pp. 174–177, 2012.
- [51] F. Dimroth and S. Kurtz, “High-Efficiency Multijunction Solar Cells,” *MRS Bull.*, vol. 32, no. 3, pp. 230–235, Mar. 2007.
- [52] R. R. King *et al.*, “Band gap-voltage offset and energy production in next-generation multijunction solar cells,” *Prog. Photovolt. Res. Appl.*, vol. 19, no. 7, pp. 797–812, Nov. 2011.
- [53] “Best Research-Cell Efficiencies,” *NREL*, 2018. [Online]. Available: <https://www.nrel.gov/pv/assets/images/efficiency-chart-20180716.jpg>. [Accessed: 16-Aug-2018].
- [54] “New world record for solar cell efficiency at 46% - Fraunhofer ISE,” *Fraunhofer Institute for Solar Energy Systems ISE*. [Online]. Available: <https://www.ise.fraunhofer.de/en/press-media/press-releases/2014/new-world-record-for-solar-cell-efficiency-at-46-percent.html>. [Accessed: 16-Aug-2018].
- [55] J. C. Goldschmidt *et al.*, “Increasing the efficiency of fluorescent concentrator systems,” *Sol. Energy Mater. Sol. Cells*, vol. 93, no. 2, pp. 176–182, Feb. 2009.
- [56] C. Liu and B. Li, “Multiple dyes containing luminescent solar concentrators with enhanced absorption and efficiency,” *J. Opt.*, vol. 17, no. 2, p. 025901, 2015.
- [57] S. Chandra, M. Rafiee, J. Doran, and S. J. Mc Cormack, “Absorption coefficient dependent non-linear properties of thin film luminescent solar concentrators,” *Sol. Energy Mater. Sol. Cells*, vol. 182, pp. 331–338, Aug. 2018.
- [58] L. Luan, P. R. Sievert, B. Watkins, W. Mu, Z. Hong, and J. B. Ketterson, “Angular radiation pattern of electric dipoles embedded in a thin film in the vicinity of a dielectric half space,” *Appl. Phys. Lett.*, vol. 89, no. 3, p. 031119, Jul. 2006.
- [59] K. G. Lee *et al.*, “A planar dielectric antenna for directional single-photon emission and near-unity collection efficiency,” *Nat. Photonics*, vol. 5, no. 3, pp. 166–169, Mar. 2011.
- [60] J.-Y. Courtois, J.-M. Courty, and J. C. Mertz, “Internal dynamics of multilevel atoms near a vacuum-dielectric interface,” *Phys. Rev. A*, vol. 53, no. 3, pp. 1862–1878, Mar. 1996.
- [61] C. Chen, D.-F. Lu, R. Gao, and Z.-M. Qi, “Analysis of waveguide-coupled directional emission for efficient collection of Fluorescence/Raman light from surface,” *Opt. Commun.*, vol. 367, pp. 86–94, May 2016.
- [62] L. Luan, P. R. Sievert, W. Mu, Z. Hong, and J. B. Ketterson, “Highly directional fluorescence emission from dye molecules embedded in a dielectric layer adjacent to a silver film,” *New J. Phys.*, vol. 10, no. 7, p. 073012, 2008.
- [63] R. Connell, C. Pinnell, and V. E. Ferry, “Designing spectrally-selective mirrors for use in luminescent solar concentrators,” *J. Opt.*, vol. 20, no. 2, p. 024009, 2018.

- [64] A.-L. Joudrier, F. Proise, R. Grapin, J.-L. Pelouard, and J.-F. Guillemoles, "Modeling and Fabrication of Luminescent Solar Concentrators towards Photovoltaic Devices," *Energy Procedia*, vol. 60, pp. 173–180, Jan. 2014.
- [65] V. I. Klimov, T. A. Baker, J. Lim, K. A. Velizhanin, and H. McDaniel, "Quality Factor of Luminescent Solar Concentrators and Practical Concentration Limits Attainable with Semiconductor Quantum Dots," *ACS Photonics*, vol. 3, no. 6, pp. 1138–1148, Jun. 2016.
- [66] S. R. Wilton, M. R. Fetterman, J. J. Low, G. You, Z. Jiang, and J. Xu, "Monte Carlo study of PbSe quantum dots as the fluorescent material in luminescent solar concentrators," *Opt. Express*, vol. 22, no. 101, pp. A35–A43, Jan. 2014.
- [67] E. Hecht, *Optics*. Pearson Education, Incorporated, 2017.
- [68] J. D. Ingle and S. R. Crouch, *Spectrochemical Analysis*. Prentice Hall, 1988.
- [69] N. C. Giebink, G. P. Wiederrecht, and M. R. Wasielewski, "Resonance-shifting to circumvent reabsorption loss in luminescent solar concentrators," *Nat. Photonics*, vol. 5, no. 11, pp. 694–701, Nov. 2011.
- [70] A. Yariv, *Optical Electronics in Modern Communications*. Oxford University Press, 1997.
- [71] O. Chen *et al.*, "Synthesis of Metal–Selenide Nanocrystals Using Selenium Dioxide as the Selenium Precursor," *Angew. Chem.*, vol. 120, no. 45, pp. 8766–8769, Oct. 2008.
- [72] H. Zhao *et al.*, "Efficient and stable tandem luminescent solar concentrators based on carbon dots and perovskite quantum dots," *Nano Energy*, vol. 50, pp. 756–765, Aug. 2018.
- [73] A. A. Earp, G. B. Smith, J. Franklin, and P. Swift, "Optimisation of a three-colour luminescent solar concentrator daylighting system," *Sol. Energy Mater. Sol. Cells*, vol. 84, no. 1, pp. 411–426, Oct. 2004.
- [74] M. J. Currie, J. K. Mapel, T. D. Heidel, S. Goffri, and M. A. Baldo, "High-Efficiency Organic Solar Concentrators for Photovoltaics," *Science*, vol. 321, no. 5886, pp. 226–228, Jul. 2008.
- [75] L. H. Slooff *et al.*, "A luminescent solar concentrator with 7.1% power conversion efficiency," *Phys. Status Solidi RRL – Rapid Res. Lett.*, vol. 2, no. 6, pp. 257–259, Dec. 2008.
- [76] C. Pu and X. Peng, "To Battle Surface Traps on CdSe/CdS Core/Shell Nanocrystals: Shell Isolation versus Surface Treatment," *J. Am. Chem. Soc.*, vol. 138, no. 26, pp. 8134–8142, Jul. 2016.
- [77] R. K. Čapek *et al.*, "Optical Properties of Zincblende Cadmium Selenide Quantum Dots," *J. Phys. Chem.*, vol. 114, no. 14, pp. 6371–6376, Mar. 2010.
- [78] S. Kirner *et al.*, "An improved silicon-oxide-based intermediate-reflector for micromorph solar cells - Kirner - 2012 - physica status solidi c - Wiley Online Library," *Phys. Status Solidi C*, vol. 9, no. 10–11, pp. 2145–2148, 2012.
- [79] P. Buehlmann *et al.*, "In situ silicon oxide based intermediate reflector for thin-film silicon micromorph solar cells," *Appl. Phys. Lett.*, vol. 91, no. 14, p. 143505, Oct. 2007.

- [80] D. Dominé, P. Buehlmann, J. Bailat, A. Billet, A. Feltrin, and C. Ballif, “Optical management in high-efficiency thin-film silicon micromorph solar cells with a silicon oxide based intermediate reflector,” *Phys. Status Solidi RRL – Rapid Res. Lett.*, vol. 2, no. 4, pp. 163–165, Aug. 2008.
- [81] T. Söderström, F.-J. Haug, X. Niquille, V. Terrazzoni, and C. Ballif, “Asymmetric intermediate reflector for tandem micromorph thin film silicon solar cells,” *Appl. Phys. Lett.*, vol. 94, no. 6, p. 063501, Feb. 2009.
- [82] F.-J. Haug, M. Boccard, R. Biron, B. Niesen, M. Despeisse, and C. Ballif, “Advanced intermediate reflector layers for thin film silicon tandem solar cells,” 2013.
- [83] R. B. Wehrspohn and J. Üpping, “3D photonic crystals for photon management in solar cells,” *J. Opt.*, vol. 14, no. 2, p. 024003, 2012.
- [84] J. Üpping *et al.*, “Three-Dimensional Photonic Crystal Intermediate Reflectors for Enhanced Light-Trapping in Tandem Solar Cells,” *Adv. Mater.*, vol. 23, no. 34, pp. 3896–3900, Sep. 2011.
- [85] H.-H. Hsiao, C. H. Chu, and D. P. Tsai, “Fundamentals and Applications of Metasurfaces,” *Small Methods*, vol. 1, no. 4, p. 1600064, Apr. 2017.
- [86] A. F. Koenderink, A. Alù, and A. Polman, “Nanophotonics: Shrinking light-based technology,” *Science*, vol. 348, no. 6234, pp. 516–521, May 2015.
- [87] N. Yu and F. Capasso, “Flat optics with designer metasurfaces,” *Nat. Mater.*, vol. 13, no. 2, pp. 139–150, Feb. 2014.
- [88] T. P. Steinbusch, H. K. Tyagi, M. C. Schaafsma, G. Georgiou, and J. G. Rivas, “Active terahertz beam steering by photo-generated graded index gratings in thin semiconductor films,” *Opt. Express*, vol. 22, no. 22, pp. 26559–26571, Nov. 2014.
- [89] Z. Li, K. Yao, F. Xia, S. Shen, J. Tian, and Y. Liu, “Graphene Plasmonic Metasurfaces to Steer Infrared Light,” *Sci. Rep.*, vol. 5, p. 12423, Jul. 2015.
- [90] F. Xiao, W. Hu, and A. Xu, “Optical phased-array beam steering controlled by wavelength,” *Appl. Opt.*, vol. 44, no. 26, pp. 5429–5433, Sep. 2005.
- [91] O. Wolf *et al.*, “Phased-array sources based on nonlinear metamaterial nanocavities,” *Nat. Commun.*, vol. 6, p. 7667, Jul. 2015.
- [92] M. I. Shalaev, J. Sun, A. Tsukernik, A. Pandey, K. Nikolskiy, and N. M. Litchinitser, “High-Efficiency All-Dielectric Metasurfaces for Ultracompact Beam Manipulation in Transmission Mode,” *Nano Lett.*, vol. 15, no. 9, pp. 6261–6266, Aug. 2015.
- [93] J. Cheng, D. Ansari-Oghol-Beig, and H. Mosallaei, “Wave manipulation with designer dielectric metasurfaces,” *Opt. Lett.*, vol. 39, no. 21, pp. 6285–6288, Nov. 2014.